Long-term non-isothermal reactive transport model of compacted bentonite, concrete and corrosion products in a HLW repository in clay

Alba Mon, Javier Samper, Luis Montenegro, Acacia Naves & Jesús Fernández

Centro de Investigaciones Científicas Avanzadas (CICA). E.T.S.I Caminos, Canales y Puestos. Universidade da Coruña. Campus de Elviña, University of A Coruña, 15071 La Coruña, Spain, j.samper@udc.es

Abstract. Radioactive waste disposal in deep geological repositories envisages engineered barriers such as carbon-steel canisters, compacted bentonite and concrete liners. The stability and performance of the bentonite barrier could be affected by the corrosion products at the canister-bentonite interface and the hyper-alkaline conditions caused by the degradation of concrete at the bentonite-concrete interface. Additionally, the host clay formation could also be affected by the hyper-alkaline plume at the concrete-clay interface. Here we present a non-isothermal multicomponent reactive transport model of the long-term (1 Ma) interactions of the compacted bentonite with the corrosion products of a carbon-steel canister and the concrete liner of the engineered barrier of a high-level radioactive waste repository in clay. Model results show that magnetite is the main corrosion product. Its precipitation reduces significantly the porosity of the bentonite near the canister. The degradation of the concrete liner leads to the precipitation of secondary minerals and the reduction of the porosity of the bentonite and the clay formation at their

interfaces with the concrete liner. The reduction of the porosities becomes especially relevant at t = 10^4 years. The zones affected by pore clogging at the canister-bentonite and concrete-clay interfaces at 1 Ma are approximately equal to 1 and 3.3 cm thick, respectively. The hyper-alkaline front (pH > 8.5) spreads 2.5 cm into the clay formation after 1 Ma. Our simulation results share the key features of the models reported by others for engineered barrier systems at similar chemical conditions, including: 1) Pore clogging at the canister-bentonite and concrete-clay interfaces; 2) Narrow alteration zones; and 3) Limited smectite dissolution after 1 Ma.

Keywords. Reactive transport, compacted bentonite barrier, corrosion products, concrete, radioactive waste disposal, hyper-alkaline pH front, CORE^{2D}

1. Introduction

Carbon steel, compacted bentonite and concrete have been proposed as candidate materials for the engineered multi-barrier system of deep geological repositories (DGR) for high-level radioactive waste (HLW) in clay formations. Carbon steel and compacted bentonite can be used as overpack and buffer, respectively, while concrete and cement are used for mechanical support in shotcrete, tunnel seals and plugs.

The interaction of cementitious materials with the clay host rock produces a hyper-alkaline fluid (10 < pH < 13.5) which can interact with the initially unsaturated bentonite surrounding the carbon steel canister (Yang *et al.*, 2008a). The physical and chemical properties of the bentonite and the clay host rock could be affected by this hyper-alkaline fluid. This interaction could produce high pH in the bentonite and in the clay, cause mineral dissolution and precipitation of secondary minerals, reduce the porosities of the bentonite buffer and the host rock, and lead to a loss of swelling capacity and radionuclide sorption capacity. In addition, the corrosion of the carbon steel and the formation

of corrosion products could induce bentonite alterations, resulting in changes in bentonite porosity, permeability, sorption, swelling and pH (Samper *et al.*, 2016).

Extensive experimental studies and numerical models of the iron-bentonite interactions and the effects of corrosion products on the bentonite have been performed in recent years (Montes-H *et al.*, 2005; Bildstein *et al.*, 2006; Wersin *et al.*, 2007; Samper *et al.*, 2008a; Savage *et al.*, 2010a; Marty *et al.*, 2010a,b; Lu *et al.*, 2011, Ngo *et al.*, 2014, Samper *et al.*, 2016). Some numerical models predict that magnetite will be the main corrosion product (Samper *et al.*, 2008a; Lu *et al.*, 2011, Samper *et al.*, 2016) while others predict also the formation of Fe-bearing aluminosilicates (Wersin *et al.*, 2007; Savage *et al.*, 2010a; Marty *et al.*, 2010a; Ngo *et al.*, 2014).

Some geochemical reactions such as smectite dissolution are often ignored in short to medium-term geochemical models because they can be disregarded in the short term. Savage *et al.* (2010c) studied the potential contribution of the smectite hydrolysis to the long term geochemical processes in a KBS-3 bentonite buffer. They concluded that smectite dissolution could be significant for the future geochemical state of a buffer, but the time scale of this process is too long for experimental verification. The relevance of smectite dissolution for a repository in granite was evaluated by Samper *et al.* (2016). The cumulative amount of smectite dissolution after 1 Ma in a repository in a granitic formation is equal to 2 % (vol). Smectite dissolution has the beneficial effect of leading to a slight decrease (1 cm) of the thickness of the altered bentonite zone (Johnson *et al.*, 2014; Samper *et al.*, 2016).

The long-term interactions of cement-claystone barriers have been studied by laboratory experiments and industrial and natural analogues (Savage *et al.*, 1992; Bauer and Berger, 1998; Steefel and Lichtner, 1998; De Windt *et al.*, 2004; Soler *et al.*, 2004; Tinseau *et al.*, 2006; Yang *et*

al., 2008a; Fernández *et al.*, 2009b; Savage, 2011; Savage *et al.*, 2011; Berner *et al.*, 2013; Kosakowski and Berner, 2013; Shao *et al.*, 2013; Watson *et al.*, 2013; 2016). Extensive reactive transport modelling studies of the long-term cement-bentonite interactions and the effects of the hyperalkaline plume have been performed during the last 25 years (Fritz and Madé, 1991; Savage *et al.*, 2002; 2010b; Watson *et al.*, 2007; 2009a; 2009b; Ueda *et al.*, 2007; Yamaguchi *et al.*, 2007; Fernández *et al.*, 2009a; Marty *et al.*, 2009, 2010a; Lehikoinen, 2009; Savage, 2012).

Shao *et al*. (2013) performed reactive transport simulations of the Maqarin marl rock natural analogue for 500 years with a 1-D model by using the OpenGeoSys-GEM code. Their results show pore clogging with the precipitation of ettringite and CSH phases in the marl rock exposed to the hyperalkaline plume in a band of 0.5 to 1 cm. According to the numerical model, the pores of the clay rock formation become clogged after $2 \cdot 10^4$ years. Watson *et al.* (2016) presented reactive transport simulations of the mineral-fluid interactions along the fractures of the Maqarin analogue and concluded that the fracture sealing is likely to occur when hyperalkaline fluids derived from cement degradation come into contact with rocks saturated with neutral pH and bicarbonate-rich groundwaters.

Kosakowski and Berner (2013) presented numerical reactive transport calculations to evaluate the geochemical evolution at cement/clay interfaces for different transport scenarios through several Opalinus clay rocks for a time span of $2 \cdot 10^3$ years. High pH, mineralogical and porosity changes are restricted to narrow zones for all host rocks. The clogging of the pore space leads to a strong reduction of diffusive fluxes across the interface, which stops the geochemical alteration processes and significantly slows down mass transport across the interface.

Berner *et al*. (2013) presented the simulations of the interactions of a MX-bentonite buffer with a low-pH concrete and the Opalinus Clay. Calculations were performed for $3 \cdot 10^4$ years with the OpenGeoSys-GEM code. Their results show that the thickness of the zone containing significant mineralogical alterations is at most a few cents of mm in both the bentonite and the Opalinus Clay adjacent to the liner. The precipitation of minerals reduces the porosity near the bentonite-concrete and concrete-Opalinus Clay interfaces. The effect is more pronounced and faster at the concrete liner-Opalinus Clay interface. The simulations reveal that significant pH changes in the bentonite and the Opalinus Clay are limited to zones less than 10 cm thick after $3 \cdot 10^4$ years.

Watson *et al.* (2013) performed a reactive transport modelling of a cement-clay interface at the industrial analogue of Tournemire (France) by using QPAC, the Quintessa's general-purpose modelling software. The sample overcoring and extraction in boreholes filled with concrete and cement, which have had remained in contact with the natural mudstone for 15-20 years, allowed the mineralogical characterization of the alterations observed around the concrete-mudstone interface. In the concrete and in the mudstone there is a general increase in porosity while there is a reduction in porosity at both sides of the concrete-mudstone interface. Watson *et al.* (2013) concluded that the inclusion of the cation exchange in the base model reduces the extent of the hyperalkaline plume in the mudstone. However, the pH profile is almost unaffected when protonation/deprotonation reactions on the montmorillonite surface are considered in the model.

Yang *et al.* (2008a) presented a numerical model of water flow, heat transfer and multicomponent reactive solute transport to evaluate the long-term geochemical evolution in the bentonite barrier, the concrete and the clay formation for a potential geological radioactive waste repository in a clay formation. Calculations were performed for 1 Ma by using the CORE^{2D} V4 code. They concluded that: 1) The dissolution of the CSH minerals in the concrete causes an increase in pH to 13; 2) The

porosity of the bentonite buffer decreases from 0.4 to 0.3; and 3) The hyperalkaline plume from the concrete migrates 70 cm into the clay formation over the time range of 1 Ma.

Here we present a non-isothermal multicomponent reactive transport model to study the long-term geochemical interactions of compacted bentonite with the concrete liner and the corrosion products in a HLW repository in a clay formation for 1 Ma. Our non-isothermal reactive transport greatly extends the scope of the model of Yang *et al.* (2008a) by accounting simultaneously for canister corrosion and concrete degradation and incorporating additionally: 1) Surface complexation on three types of sorption sites; 2) Iron sorption by surface complexation; 3) Kinetic smectite dissolution; and 4) Precipitation of secondary clay minerals.

2. Reactive transport model

2.1 Conceptual model

The model corresponds to a radioactive waste repository in clay according to the Spanish Reference Concept (ENRESA, 2004) (Fig. 1). Cylindrical carbon steel canisters with 0.9m diameter are emplaced in horizontal galleries and embedded into a 0.75 m thick bentonite buffer. A 0.3 m thick concrete sustainment is located between the bentonite buffer and the clay formation (Fig. 2).

Heat and solute transport processes are assumed to have axial symmetry with respect to the axis of the galleries. Therefore, the model is discretized with a one-dimensional axisymmetric grid which accounts for the canister, the bentonite, the concrete and the clay formation. The model domain extends up to a radial distance of 25 m from the axis of the disposal gallery.

Similar to Yang *et al.* (2008a), the simulation starts (t = 0) when the bentonite buffer is fully saturated. According to Zheng and Samper (2008), the bentonite barrier will become fully saturated

50 years after the barrier emplacement. The numerical model accounts for the thermal transient stage and the cooling of the radioactive waste. Fig. 3 shows the time evolution of the temperature prescribed at the canister-bentonite interface (r = 0.45 m), the bentonite-concrete interface (r = 1.2 m), the concrete-clay interface (r = 1.5 m) and the outer boundary (r = 25 m). These temperatures were taken from the calculations performed for the performance assessment of a HLW repository in clay according to the Spanish Reference Concept (ENRESA, 2004). The temperature in the canister is about 98ºC for t < 10 years. Then, it decreases to 45 ºC at t = 10^4 years and reaches 19.7 ºC at 1 Ma. The maximum temperature at the bentonite-concrete is 75.8ºC at t = 10 years. The maximum temperature at r = 25 m is 42 ºC at 10^3 years.

The model accounts for canister corrosion, aqueous complexation, acid/base, redox reactions, mineral dissolution/precipitation, surface complexation of Fe^{2+} and H^+ on three types of sorption sites (S^SOH, $S^{W1}OH$ and $S^{W2}OH$) and cation exchange reactions of Ca^{2+}, Mg^{2+}, Na^+, K^+ and Fe^{2+}. The chemical system is defined in terms of the following 13 primary species: H_2O, H^+, Ca^{2+}, Mg^{2+}, Na^+, K^+, Cl^-, SO_4^{2-}, HCO_3^-, $SiO_2(aq)$, $O_2(aq)$, Fe^{2+} and $AlOH_4^-$. The model considers 17 minerals and 58 aqueous complexes identified from speciation runs performed with EQ3/6 (Wolery, 1992) (see Table 1). Cation exchange reactions are modeled with the Gaines-Thomas convention (Gaines & Thomas, 1953). The triple sorption site model of Bradbury and Baeyens (1997; 2005) is used to model surface complexation reactions. Chemical reactions and their equilibrium constants at 25 ºC for aqueous species and mineral dissolution/precipitation as well as selectivity coefficients for exchanged cations and protolysis constants for surface complexation are listed in Table 1.

Dissolved oxygen will be consumed soon after repository closure. Therefore, anaerobic conditions will prevail in the long term. Canister corrosion is assumed to proceed according to:

$$Fe(s) + 2H_2O \rightleftarrows Fe^{2+} + 2OH^- + H_2(g) \quad (1)$$

Similar to Samper *et al.* (2016), this reaction is rewritten in terms of the primary species used in the numerical model:

$$Fe(s) + 2H^+ + 0.5O_2(aq) \rightleftarrows Fe^{2+} + H_2O \quad (2)$$

All the reactions except for canister corrosion and smectite dissolution are assumed at chemical equilibrium.

Kinetic mineral dissolution/precipitation is modelled with the following kinetic rate law (Samper *et al.*, 2000):

$$r_m = s_m k_m e^{\frac{-Ea}{RT}} \left(\prod_{i=1}^{N_T} a_i^{p_{mi}}\right) \left(\Omega_m^{\theta} - 1\right)^{\eta} \quad (3)$$

where r_m is the dissolution/precipitation rate (mol/m^2/s), k_m is the kinetic rate constant (mol/m^2/s) at 25ºC, Ea is the activation energy, R is the gas constant, T is the temperature (K), Ω_m is the saturation index which is equal to the ratio of the ion activity product to the equilibrium constant (dimensionless), Θ and η are empirical parameters, s_m is equal to -1 for precipitation and 1 for dissolution, and $\prod_{i=1}^{N_T} a_i^{p_{mi}}$ is a catalytic term which accounts for the activities a_i of the aqueous species and p_{mi} is the exponent for the i-th aqueous species in the m-th mineral phase.

The dissolution/precipitation rate in mol/m^2/s, r_m, is multiplied by the mineral specific surface area, σ, to get the dissolution/precipitation rate in mol/m^3/s, R_m. The specific surface area σ is defined as the surface area of the mineral per unit fluid volume. The model assumes that σ is constant and independent of the mineral molar volume.

The carbon steel corrosion rate, r_c, in μm/year is calculated as:

$$r_c = \frac{r_m M_w}{\rho} \tag{4}$$

where r_m is the corrosion rate per unit mineral surface (mol/m^2/year), ρ is the density of the carbon steel (7860 kg/m^3), and M_w is its molecular weight (55.85 g/mol). The corrosion rate is constant and equal to 2 μm/year (Samper *et al.*, 2016), which amounts to 0.281 mol/m^2/year. It should be noticed that η in Eq. (3) is equal to zero for constant canister corrosion.

Smectite dissolution was simulated by assuming the chemical formulation of the FEBEX-montmorillonite derived by Fernández *et al.* (2009a) (Table 1) and by using the following kinetic rate law (Sánchez *et al.*, 2006):

$$r_m = -k_m a_{OH}^n e^{-\frac{Ea}{RT}} \tag{5}$$

where Ea is equal to 22.7 KJ/mol, k_m is equal to 2·10^{-13} mol/s/m^2, a_{OH}^n is a catalytic term which depends on the activity of the OH^- and n is an exponent which is equal to 0.5. The smectite specific surface area, σ, is assumed equal to 100 dm^2/L (Fernández *et al.*, 2009a).

2.2 Numerical model

A 1-D axisymmetric numerical model was used to simulate the long-term geochemical interactions of compacted bentonite with concrete and corrosion products in a HLW repository in a clay formation with a total length of 25 m (Fig. 2). The finite element grid contains non-uniform 1D line elements with 8 elements in the canister, 31 in the bentonite, 31 in the concrete and 78 in the clay host rock. The grid size is constant in the canister with Δr = 1.25 cm. The first element in the bentonite is 1 cm long. The rest of them are 2.5 cm long. The elements in the concrete range from

0.83 to 2.5 cm. In the clay formation the elements are small near the concrete interface ($\Delta r = 0.83$ cm) and increase with radial distance (Fig. 2). Similar to the model of Yang *et al.* (2008), numerical simulations were performed for a time horizon of 1 Ma. This is the time span used for the performance assessment of the Spanish radioactive waste repository in clay (ENRESA, 2004). An implicit Euler scheme was used for time integration.

Flow and transport parameters as well as the initial porewater chemical composition of the bentonite, the concrete and the clay were taken from Yang *et al*. (2008a). The initial porewater chemical composition of the canister is the same as that of the bentonite porewater.

Table 2 lists the thermal and hydrodynamic parameters of the canister, the bentonite barrier, the concrete liner and the clay formation.

The canister is made entirely of Fe(s). The model relies on the assumption that the canister has the same porosity and initial chemical composition as those of the bentonite for solving the reactive transport equations within the canister. The bentonite contains initially 0.36% (vol) of calcite, 1.19% of quartz, 0.083% of gypsum and 57.667% of smectite. The porosity of the bentonite is equal to 0.407. The concrete liner contains initially 0.1% of calcite, 1% of brucite, 16.5% of portlandite, 36.6% of tobermorite and 37.3% of nonreactive quartz. Quartz represents the inert aggregate volume fraction in the concrete and is assumed to be a non-reactive mineral. The porosity of the concrete is equal to 0.085. The clay has a porosity of 0.37. It is composed of calcite (11.3%), gypsum (1.2%), quartz (2.4%), dolomite (2.4%) and nonreactive clay mineral phases (45.7%). Nonreactive phases play no role and therefore can be disregarded. Table 1 lists the secondary minerals allowed to precipitate.

The cation exchange capacity (CEC) of the bentonite is 102 meq/100g (Fernández *et al.*, 2004). Cation selectivity coefficients for exchanged Ca^{2+}, Mg^{2+}, K^{+} and Fe^{+} (Table 1) were derived from Samper *et al.* (2008a) and Tournassat (2003). The total concentration of sorption sites in the bentonite is 0.322 mol/L. Strong sites which have a large binding affinity but a small concentration (0.0079 mol/L). The other two types are the weak #1 and #2 sites which have binding constants weaker than those of the strong sites although their concentrations (0.16 mol/L) are larger than those of the strong sites. Surface complexation and cation exchange reactions take place in the bentonite.

The temperature dependence of the equilibrium constants for aqueous complexes and minerals is calculated with the following expression which is valid for temperatures ranging from 0 to 300 ºC (Wolery, 1992):

$$\log K(T) = \frac{b_1}{T^2} + \frac{b_2}{T} + b_3 \ln T + b_4 + b_5 T \qquad (6)$$

where b_1 to b_5 are coefficients which are derived by fitting this equation to measured log K values at 0, 25, 60, 100, 150, 200, 250 and 300ºC.

The dependence of the kinetic rates on temperature is accounted for with the activation energy Ea according to Equation (3). The corrosion rate does not depend on temperature. The dependence of the corrosion rate on temperature was analyzed by Samper *et al.* (2016) for a HLW repository in granite. Their results show that the corrosion rate increases from 2 to 4.75 μm/y and then decreases smoothly reaching a value of 2.5 μm/y.

2.3 Reactive transport code

Reactive transport calculations of the long-term geochemical interactions of compacted bentonite with concrete and corrosion products in a HLW repository in a clay formation were performed with CORE^{2D} V4 (Samper *et al.*, 2009; 2011). It is a code for transient saturated and unsaturated water flow, heat transport and multicomponent reactive solute transport under both local chemical equilibrium and kinetic conditions in heterogeneous and anisotropic media. The flow and transport equations are solved with Galerkin finite elements and an Euler scheme for time discretization. The chemical formulation is based on the ion association theory and uses an extended version of Debye-Hückel equation (B-dot) for the activity coefficients of aqueous species. CORE^{2D} V4 relies on the *com* thermodynamic database of EQ3/6 (Wolery, 1992). CORE^{2D} V4 is based on the sequential iteration approach to solve for chemical reactive solute transport. Iterations are repeated until prescribed convergence criteria are attained (Xu *et al.*, 1999). The code has been used to model laboratory and in situ experiments (Molinero and Samper, 2004; Dai *et al.*, 2008; Samper *et al.*,2008b; Soler *et al.*, 2008; Zhang *et al.*, 2008; Zheng and Samper, 2008; Yang *et al.*, 2008b; Zheng *et al.*, 2010; 2011), to model the interactions of corrosion products and bentonite (Samper *et al.*, 2008a; Lu *et al.*, 2011), to evaluate the long-term geochemical evolution of repositories in granite and clay (Yang *et al.*, 2008a, Samper *et al.*, 2016), and to model the impact of CO_2 leakage on groundwater quality (Yang *et al.*, 2013, 2015).

3. Model results and discussion

3.1. pH and dissolved species

Solute concentrations and pH of porewaters in the system are mostly affected by: 1) Solute diffusion from the bentonite into the concrete because the initial concentrations of major ions in concrete are smaller than those in bentonite; and 2) Mineral dissolution/precipitation caused by the spreading of the hyperalkaline plume from the concrete into the bentonite buffer and the clay formation.

The time evolution of the numerical results are shown at some selected nodes located at or near the interfaces. The first point at r = 0.45 m is located at the bentonite-canister interface. The second point at r = 1.125 m is located in the bentonite at 7.5 cm from the bentonite-concrete interface. The third point at r = 1.35 m is the midpoint of the concrete. The fourth point at r = 1.525 m is in the clay formation at 2.5 cm from the concrete-clay interface.

The pH at the canister-bentonite interface increases until $8 \cdot 10^4$ years due to the canister corrosion and reaches a maximum of 12.4. Then, the pH decreases when the corrosion finishes (Fig. 4). The pH in the bentonite is affected by the canister corrosion and the hyperalkaline fronts. The pH in the bentonite near the concrete interface increases faster than it does at the bentonite-canister interface because the pH is affected by the hyperalkaline plume from the concrete more strongly than it is from canister corrosion. The pH in the bentonite increases radially outwards from the canister and radially inwards from the concrete. These pH fronts spread and lead to a uniform pH equal to 12.4 at $t = 8 \cdot 10^4$ years. Then, the pH decreases when sepiolite, calcite and brucite precipitate. The pH in the concrete increases until $8 \cdot 10^4$ years when portlandite dissolves. The precipitation of sepiolite and brucite after 10^5 years leads to a decrease in pH and later also in the bentonite. The pH in the clay formation decreases from its initial value until $t = 10^2$ years when dolomite precipitates slightly as a result of the transient thermal field. Later, dolomite dissolution and the spreading of the high-pH front from the concrete lead to an increase in pH in the clay formation. The pH in the clay near the concrete interface (r = 1.525 m) increases as a result of the hyperalkaline plume until 10^4 years

(Fig. 4). Later, it decreases when sepiolite and brucite precipitate. The pH front, considering a threshold value of 8.5 higher than the initial pH of the clay, migrates 2.5 cm into the clay formation after 1 Ma. Fig. 5 shows the contour plot of the computed pH as a function of radial distance and time. This plot shows clearly the position of the contour line pH = 8.5 which helps the visualization of the spreading of the pH fronts.

Fig. 6 to Fig. 9 show the time evolution of the computed concentrations of dissolved species in the bentonite-canister interface (r = 0.45 m), in the bentonite near the concrete interface (r = 1.125 m), in the concrete midpoint (r = 1.35 m) and in the clay formation near the concrete interface (r = 1.525 m). The concentrations of dissolved Cl^-, Na^+, Ca^{2+}, Mg^{2+}, K^+, and HCO_3^- in the bentonite decrease initially, reaching their minimum values at a time ranging from $2 \cdot 10^3$ to 10^4 years as a result of solute diffusion from the bentonite into the concrete and mineral precipitation caused by the hyperalkaline plume. The initial concentration of K^+ in the concrete is much greater than in the bentonite. The concentration of dissolved K^+ in the bentonite increases slightly for $t < 10^2$ years as a result of diffusion from the concrete where the porewater has a higher concentration of K^+ than in the bentonite. The concentration of dissolved K^+ in the bentonite porewater decreases after $t = 10^2$ years when dissolved K^+ exchanges with other interlayer cations in the bentonite.

The precipitation of calcite and tobermorite in the bentonite at early times causes a decrease in the concentration of dissolved Ca^{2+} after $t = 10^2$ years. The dissolution of brucite in the bentonite which had precipitated previously leads to an increase in the concentration of dissolved Mg^{2+} at $t = 8 \cdot 10^4$ years. The concentration of dissolved Fe^{2+} at the bentonite-canister interface increases due to canister corrosion. Later, it decreases when magnetite precipitates. The strong decrease of the concentration of dissolved Fe^{2+} at $t = 5 \cdot 10^4$ years is associated with the previous increase of the concentration of iron sorbed on the strong sorption sites. The concentration of dissolved aluminium

in the bentonite increases when smectite dissolves. Such an increase is largest in the bentonite near the concrete interface. The concentration of dissolved silica increases when quartz dissolves. This leads to the precipitation of tobermorite first and sepiolite afterwards in the bentonite near the concrete interface.

The concentrations of dissolved Na^+, K^+, Ca^{2+}, HCO_3^-, SO_4^{2-}, $SiO_2(aq)$ and Cl^- in the concrete remain nearly stable (Fig. 8). The concentrations of dissolved Mg^{2+}, Fe^{2+} and aluminium increase after $t = 8 \cdot 10^4$ years as a result of solute diffusion from the bentonite, where the concentrations of these dissolved species increase also. Mineral dissolution/precipitation reactions buffer the concentrations of dissolved bicarbonate, calcium and silica in the concrete.

The concentrations of dissolved Na^+, Ca^{2+}, K^+, HCO_3^-, SO_4^{2-}, $SiO_2(aq)$ and Cl^- in the clay near the concrete interface remain equal to the initial concentrations in the clay (Fig. 9). The concentration of dissolved Mg^{2+}, Fe^{2+}, and aluminium increase with time as a result of solute diffusion from the concrete. The concentration of dissolved silica decreases in the clay near the concrete interface when sepiolite precipitates.

3.2. Minerals

Fig. 10 to Fig. 13 show the time evolution of the cumulative mineral precipitation/dissolution at the bentonite-canister interface (r = 0.45 m), in the bentonite near the concrete interface (r = 1.125 m), in the concrete midpoint (r = 1.35 m) and in the clay formation near the concrete interface (r = 1.525 m). Positive (negative) values indicate mineral precipitation (dissolution). The cumulative amount of mineral dissolution/precipitation is calculated as the difference between the concentration of the mineral at the current time t and the initial concentration.

Magnetite is the main corrosion product which precipitates near the canister-bentonite interface. Its maximum concentration is equal to 58 mol/L at $t = 5 \cdot 10^4$ years. Siderite precipitates initially. Its concentration, however, is much lower than that of magnetite (Fig. 10). Later, at $t = 10^3$ years siderite dissolves and triggers the precipitation of calcite. A small amount of analcime precipitates at $t = 2 \cdot 10^5$ years, but it redissolves soon after. Quartz dissolves initially until $t = 10^3$ years. Quartz and analcime are not shown in Fig. 10 because their concentrations are much smaller than those of the rest of the minerals. Calcite dissolves initially and precipitates when siderite dissolves. Gypsum precipitates at $t = 2 \cdot 10^5$ years. Brucite starts precipitating at $t = 10^3$ years and redissolves at $t = 2 \cdot 10^5$ years when sepiolite precipitates

Fig. 11 shows the time evolution of the concentration of the cumulative mineral precipitation/dissolution in the bentonite near the concrete interface (r = 1.125 m). Brucite precipitates here from $t = 10^2$ to $t = 2 \cdot 10^5$ years. Later, it dissolves. Sepiolite precipitates at $t = 2 \cdot 10^5$ years. Its precipitation rate increases when the dissolution of tobermorite increases the concentration of dissolved silica. Quartz dissolves until $t = 10^3$ years. Gypsum precipitates after $t = 10^5$ years when the temperature decreases. Calcite precipitates in this part of the bentonite barrier. The dissolution rate of smectite is largest near the concrete interface where the pH is highest. Analcime precipitation (not shown here) is clearly linked to the dissolution of smectite.

Fig. 12 shows the time evolution of the concentration of cumulative mineral precipitation/dissolution in the concrete midpoint. Portlandite dissolves and is exhausted at $t = 2 \cdot 10^4$ years. Tobermorite starts dissolving at $t = 9 \cdot 10^4$ years once portlandite is exhausted. The dissolution of tobermorite leads to the precipitation of calcite, gypsum, sepiolite and brucite. It should be noticed that the cumulative amount of precipitated gypsum in the concrete is much greater than that in the bentonite.

Fig. 13 shows the time evolution of the computed concentration of mineral precipitation/dissolution in the clay near the concrete interface. The increase in temperature causes the dissolution of quartz and dolomite and the precipitation of calcite. For this reason, the concentrations of some minerals in Fig. 13 do not start from zero. Brucite and gypsum precipitate. Sepiolite and calcite also precipitate, but at larger rates.

Fig. 14 shows the computed pH and mineral volume fractions at selected times. One can see the progressive precipitation of magnetite in the canister and in the bentonite near the canister interface as the canister corrosion progresses. The volume fraction of quartz in the bentonite and in the clay decreases. The tobermorite volume fraction decreases with time in the concrete and increases in the bentonite until t = 10^5 years. The portlandite volume fraction in the concrete decreases. The precipitation of gypsum refills some of the voids left by the dissolution of portlandite. Tobermorite dissolution causes the precipitation of sepiolite. Sepiolite, gypsum and brucite occupy the volume fraction previously occupied by portlandite and tobermorite at t = 1 Ma. The volume fraction of dolomite in the clay near the concrete interface decreases with time when calcite and sepiolite precipitate. Dolomite and brucite precipitate at 1 Ma in this interface and therefore the porosity of the clay decreases.

3.3 Changes in porosity

Our numerical model assumes that the porosities are constant in time. The predicted changes in porosity caused by mineral dissolution/precipitation are computed from model outputs. Fig. 1S (Supporting Material) shows the time evolution of the changes in porosity caused by mineral precipitation/dissolution. Pore clogging by magnetite precipitation is predicted at the canister-bentonite interface (r = 0.45 m) at t = $2 \cdot 10^4$ years. The porosity in the bentonite near the concrete

interface (r = 1.125 m) decreases to 0.3 when gypsum and sepiolite precipitate for $t > 2 \cdot 10^5$ years. The porosity of the concrete increases initially when portlandite dissolves. Later, it reduces to zero at $t = 1.22 \cdot 10^5$ years when gypsum and sepiolite precipitate. The simultaneous precipitation of sepiolite and calcite in the clay near the concrete interface (r = 1.525 m) leads to pore clogging at $t = 2.3 \cdot 10^5$ years. The porosity of the clay at r = 13.5 m is not affected by mineral dissolution/precipitation.

Table 3 lists the values of the thickness of bentonite and clay affected by the reduction of the porosity. The following porosity reductions are considered: 15%, 50% and 100% (clogging). The values of the thickness are provided at the canister-bentonite interface, in the bentonite near the concrete interface and in the clay near the concrete interface. The most significant reduction in porosity occurs first in the clay near the concrete interface at $t = 10^3$ years. The zone where the porosity reduces by 50% is 1.67 cm thick and the zone where the porosity reduces by 15% is 2.5 cm thick.

Pore clogging at $t = 10^4$ years occurs in a 1.67 cm zone in the clay near the concrete interface (Table 3). The zone where the porosity reduces by 50% at the canister-bentonite interface is 1 cm thick and in the clay near the concrete interface is 2.5 cm thick. The zone where the porosity reduces by 15% at the canister-bentonite interface is 1 cm thick and in the clay near the concrete interface is 2.5 cm thick.

Pore clogging at $t = 10^5$ years occurs in a 1 cm thick zone at the canister-bentonite interface and in a 1.67 cm zone in the clay near the concrete interface (Table 3). The zone where the porosity reduces by 50% at the canister-bentonite interface is 2.53 cm thick and in the clay near the concrete interface is 2.5 cm thick. The zone where the porosity reduces by 15% at the canister-bentonite interface is

5.03 cm thick and in the clay near the concrete interface is 4.17 cm thick (Fig. 2S, Supporting Material).

Pore clogging at t = 1 Ma is computed in a 1 cm thick zone at the canister-bentonite interface and in a 3.3 cm zone in the clay near the concrete interface (Table 3). The zone where the porosity reduces by 50% at the canister-bentonite interface is 2.53 cm thick and in the clay near the concrete interface is 4.17 cm thick. The zone where the porosity reduces by 15% includes most of the bentonite barrier. In the clay near the concrete interface the zone with 15% decrease in porosity is 6.67 cm thick (Fig. 3S, Supporting Material).

3.4. Cation exchange and surface complexation

Fig. 15 shows the time evolution of the concentrations of the exchanged cations. The concentration of the exchanged K^+ decreases with time after t = 10^2 years in the bentonite near the concrete interface while that of Ca^{2+} increases steadily until it reaches a maximum after t = $8 \cdot 10^4$ years. Later, the concentration of Ca^{2+} decreases sharply and stabilizes at a value of 20 meq/100 g. The trend of the concentration of Mg^{2+} is opposite to that of Ca^{2+}. The concentration of exchanged Mg^{2+} decreases initially and becomes negligible at t = 10^3 years. It remains very small until t = $2 \cdot 10^5$ years. Later, it increases sharply and stabilizes at a value of 56 meq/100 g. The concentration of exchanged Fe^{2+} is small.

Fig. 4S (Supporting Material) shows the time evolution of the computed concentrations of the sorbed species on strong, weak #1 and weak #2 sites in the bentonite near the concrete interface (r = 1.125 m). S^sOFe^+ is the main sorbed species on the strong sites until t = 10^2 years. Later, the concentration of S^sOFe^+ decreases and that of S^sO^- increases. $S^sOFe(OH)_2^-$ is the dominant species for $10^4 < t < 10^5$ years. Finally, S^sO^- becomes again the dominant sorbed species on strong sites.

$S^{w1}O^-$ is the main sorbed species on the weak #1 sites after $t = 5 \cdot 10^3$ years. Iron sorption on the weak sites is not relevant. $S^{w2}O^-$ and $S^{w2}OH$ are the dominant sorbed species on the weak #2 sites. The concentration of $S^{w2}O^-$ is the largest for $t < 6 \cdot 10^2$ and $t > 3 \cdot 10^5$ years. The dominant sorbed species at t = 1 Ma are $S^{w1}O^-$ and $S^{w2}OH$. Their concentrations are uniform throughout the bentonite barrier.

4. Effect of grid size on the numerical solution

The zones of bentonite and clay suffering the effects of canister corrosion and concrete degradation are narrow. Their quantification requires proper spatial discretization schemes (Marty *et al.*, 2009; Hayek *et al.*, 2011). In this section, we explore the effects of the grid size on the computed geochemical evolution of the system, the pH, the mineral volume fractions and the changes in porosity and pore clogging. Fig. 5S to Fig. 8S (Supporting Material) show the pH and mineral volume fractions computed with a fine, an intermediate and a coarse grid having 148, 108 and 66 elements, respectively. The mineral volume fractions and the pH computed with the fine and intermediate grids are generally similar. The mineral volume fractions and the pH computed with the coarse grid show significant differences compared to those computed with the intermediate and fine grids. The differences are especially substantial for tobermorite and portlandite in the concrete and sepiolite and gypsum in the clay near the concrete interface for $t < 10^4$ years. These differences occur also in the bentonite for $t > 10^4$ years. The spreading of the high pH front in the clay formation with the coarse grid is larger than that of the fine grid.

Fig. 9S to Fig. 12S (Supporting Material) show the changes in porosity computed with the fine, intermediate and coarse grids. The porosities computed with the fine and intermediate grids are similar almost always. The zones of bentonite and clay affected by a reduction of porosity computed

with the coarse grid are significantly wider than those computed with the intermediate and fine grids. The numerical errors of the coarse grid are largest at t = 1 Ma.

5. Sensitivity Analysis

A comprehensive sensitivity analysis was performed to study the uncertainties in the geochemical model and the model parameters. This analysis leads to conclusions similar to those reported by Samper *et al.* (2016) for the engineered barrier system of a HLW repository in granite. Here we report only the results of the sensitivities which address the relevance of: 1) Cation exchange selectivities; 2) Surface complexation; 3) Kinetic smectite dissolution and analcime precipitation; 4) Mg-saponite precipitation; and 5) The separated contributions of canister corrosion and concrete degradation to bentonite alteration.

To reduce the computing time required for the sensitivity runs and be consistent with the grid sizes used by Yang *et al.* (2998a) and Samper *et al.* (2016), the sensitivity runs presented here were computed with the coarse grid having 66 elements.

5.1 Cation exchange selectivities

A sensitivity run was performed to evaluate the sensitivity of the model predictions to changes in cation selectivities (Table 1). The selectivity coefficients of Ca^{2+}, Mg^{2+} and K^{+} reported by Yang *et al.* (2008a) were used in the sensitivity run. The concentrations of dissolved species, the pH and mineral dissolution/precipitation lack sensitivity to the selectivity coefficients. The concentrations of the exchanged Ca^{2+}, Mg^{2+} and Na^{+} in the bentonite near the concrete interface (r = 1.125 m), however, are sensitive to changes in the selectivity coefficients (Fig. 15). The general trends of the

exchanged concentrations are similar in both runs. The concentration of exchanged Ca^{2+} in the base run is greater than that of the sensitivity run. The concentration of exchanged K^{+} in the base run, however, is lower than that of the sensitivity run.

5.2 Sensitivity to surface complexation

The relevance of surface complexation reactions was evaluated with a sensitivity run in which iron and proton surface complexation reactions in the bentonite were disregarded. This run accounts for proton exchange in a manner similar to Yang *et al.* (2008a). Fig. 13S (Supporting Material) shows that the radial distribution of the computed the pH at 1 Ma in the sensitivity run is nearly the same as that of the base run. This result is consistent with the results of Watson *et al.* (2013) who found that the breakthrough of the pH front (pH > 8.5) in the clay is not sensitive to surface complexation reactions. The computed concentrations of dissolved species and minerals are also similar in both runs. However, the computed magnetite precipitation at the canister-bentonite interface in the sensitivity run for $t > 2 \cdot 10^4$ years is slightly larger than that of the base run because in this run Fe^{2+} is sorbed by surface complexation in the base run (see Fig. 14S, Supporting Material).

5.3 Sensitivity to smectite dissolution and analcime precipitation

Smectite dissolution is commonly disregarded in short to medium-term geochemical models (e.g. lab and in-situ tests) because it is not considered relevant in the short term. However, this reaction could be relevant for the long-term geochemical evolution of the engineered barrier system (Savage *et al.*, 2010c). To assess its relevance, a sensitivity run was performed by disregarding smectite dissolution and analcime precipitation in the bentonite barrier. The computed pH in the bentonite at t = 1 Ma in the sensitivity run is slightly lower than that of the base run (Fig. 13S, Supporting

Material). In addition, the breakthrough of the pH front (pH > 8.5) in the clay in the sensitivity run is 15 cm, clearly smaller than that of the base run (35 cm). Computed results of dissolved, exchanged and sorbed species are similar in both runs. Brucite precipitation in the bentonite near the concrete interface (r = 1.125 m) and in the concrete (r = 1.35 m) in the sensitivity run is larger than that of the base run while gypsum precipitation in these places in the sensitivity run is lower than that of the base run. The computed porosity in the sensitivity run is smaller than that of the base run from $5 \cdot 10^4$ to $3 \cdot 10^5$ years because of brucite precipitation. The computed porosity at t = 1 Ma is the same in both runs.

5.4 Sensitivity to Mg-saponite precipitation

A sensitivity run was performed which accounts for kinetic Mg-saponite precipitation in the bentonite. The precipitation rate, r_m, was calculated with Eq. (3) with $k_m = 10^{-9}$ mol/m^2/s, Ea = 41.86 KJ/mol, $\eta = 1$ and $\theta = 1$ (Fernández *et al.*, 2009a). The specific surface, σ, of Mg-saponite was taken equal to 10^{-10} dm^2/L.

The computed pH at t = 1 Ma in the sensitivity run with Mg-saponite precipitation is slightly larger than that of the base run (Fig. 13S, Supporting Material). The cumulative magnetite precipitation at the canister-bentonite interface (r = 0.45 m) in the sensitivity run is slightly smaller than that of the base run (Fig. 14S, Supporting Material). Mg-saponite precipitation tends to slow down smectite dissolution (Fig. 15S, Supporting Material).

5.5 Sensitivity to concrete degradation and canister corrosion

To assess the separate contributions of concrete degradation and canister corrosion to the alteration of the bentonite barrier, a detailed comparison of the computed pH was performed for the following

three cases: 1) A model with bentonite (B), and concrete (C) degradation, but no canister corrosion. This model is denoted here as B-C model; 2) A model with canister corrosion (C), bentonite (B) and concrete (C) degradation which is denoted as C-B-C model; and 3) A model with canister corrosion (C) and bentonite (B), but no concrete degradation. The B-C model is similar to the model reported by Yang *et al.* (2008a). The C-B-C model corresponds to the model presented here and the C-B model has been reported by Samper *et al.* (2016).

The radial distribution of the computed pH at t = 10^3 shows clearly the hyperalkaline pH front in the B-C and C-B-C models and the increase in pH near the canister due to canister corrosion in the C-B model (Fig. 16). The pH computed with the C-B model shows a sharp decrease at r = 0.47 m when Fe^{2+} sorbs on weak #1 sites (Samper et al, 2016). Such a sharp drop in pH is not computed with the C-B-C model.

The computed pH at t = 10^4 years shows that the hyperalkaline pH front in the B-C and C-B-C models spreads into the bentonite barrier (Fig. 16). The pH computed with the C-B-C model near the canister is lower than that of the B-C model (no corrosion) because the high pH promotes magnetite precipitation. The pH computed with the C-B model decreases sharply at r = 0.54 m when Fe^{2+} sorbs on weak #1 sites. The pH computed with the C-B-C model is larger than the pH computed with the C-B model.

The computed pH becomes uniform for t $\geq 10^5$ years. The computed pH at t = 10^5 years is equal to 11 for the B-C and C-B-C models and 9.3 for the C-B model. At t = 1 Ma the pH is equal to 9.5 for the B-C and C-B-C models and 8.7 for the C-B model.

6. Comparison with the results of other models

Similar to Shao *et al.* (2013) who found that pore clogging occurs in the clay formation after $2 \cdot 10^4$ years, our model predicts pore clogging in the clay formation at around $t = 10^4$ years. Our calculations share the features of the results of Kosakowski and Berner (2013) such as narrow alteration zones with pore clogging. Similar to Berner *et al.* (2013), our results show that smectite dissolution is very small. The model of Berner *et al.* (2013) predicts that the pH front spreads about 10 cm in the clay formation after $3 \cdot 10^4$ years. The pH front in our model reaches around 4.17 cm after $t = 10^4$ years. The front of high pH migrates 2.5 cm after 1 Ma. The results of our sensitivity run without surface complexation reactions are consistent with the findings of Watson *et al.* (2013) who reported that the breakthrough of the pH front (pH > 8.5) in the clay formation is not sensitive to surface complexation reactions.

7. Summary and conclusions

A non-isothermal multicomponent reactive transport model of the long-term (1 Ma) interactions of the compacted bentonite with the corrosion products of a carbon-steel canister and the concrete liner of the engineered barrier of a high-level radioactive waste repository in clay has been presented. The numerical results show that magnetite is the main corrosion product. Its precipitation reduces the bentonite porosity near the canister. Concrete degradation leads to the precipitation of secondary minerals and the reduction of the porosity of the bentonite and the clay formation at their interfaces with the concrete liner. The decrease of the porosities is especially important for $t > 10^4$ years. The zones affected by pore clogging at the canister-bentonite, and concrete-clay interfaces at 1 Ma are equal to 1, and 3.3 cm thick, respectively. The pH in the bentonite after 1 Ma is uniform and equal to 9.42. At that time, the hyperalkaline front (pH > 8.5) migrates 2.5 cm into the clay formation.

Sensitivity runs were performed to analyse the uncertainties in cation exchange selectivities and evaluate the relevance of surface complexation reactions, kinetic smectite dissolution, and Mg-saponite precipitation. Only the concentrations of the exchanged Ca^{2+}, Mg^{2+} and Na^{+} and K^{+} are sensitive to changes in the selectivity coefficients. The computed pH at t = 1 Ma in the sensitivity run without surface complexation reactions is the same as that of the base run. Accounting for smectite dissolution leads to: 1) Slight changes in the computed pH in the bentonite at t = 1 Ma; 2) A reduction in the breakthrough of the pH front into the clay formation from 35 to 15 cm; 3) An increase in brucite precipitation in the bentonite near the concrete interface and in the concrete; and 4) A decrease of gypsum precipitation. The run with Mg-saponite precipitation in the bentonite leads to slightly larger pH, slightly smaller magnetite precipitation and smaller smectite dissolution at t = 1 Ma.

The results of our simulations show similarities with the results of the models reported by others for engineered barrier systems at similar chemical conditions, including: 1) Pore clogging at the canister-bentonite and concrete-clay interfaces; 2) Narrow alteration zones; and 3) Limited smectite dissolution after 1 Ma.

The results of the long-term geochemical predictions presented here could be improved by: 1) Accounting for the feedback on porosity and other transport and chemical parameters caused by mineral precipitation/dissolution; and 2) Simulating canister corrosion in a more realistic manner by adopting a dynamic corrosion front.

Acknowledgements

The research leading to this work has received funding from the PEBS Project of the European Atomic Energy Community's Seventh Framework Programme (FP7/2007-2011) under grant agreement 232598. This work was partly funded by ENRESA (Spain), the Spanish Ministry of Economy and Competitiveness (Projects CGL2012-36560 and CGL2016-78281), FEDER funds and the Galician Regional Government (Project 10MDS118028PR and Fund 2012/181 from *"Consolidación e estruturación de unidades de investigación competitivas", Grupos de referencia competitiva*). The first author enjoyed a research contract from University of A Coruña and the fifth author had a Contract from the FPI Program of the Spanish Ministry of Economy and Competitiveness.

References

Bauer, A., Berger, G., 1998. Kaolinite and smectite dissolution rate in high molar KOH solutions at 35° and 80 °C. Applied Geochemistry13, 905–916.

Berner, U., Kulik, D. A., Kosakowski, G., 2013. Geochemical impact of a low-pH cement liner on the near field of a repository for spent fuel and high-level radioactive waste. Physics and Chemistry of the Earth 64, 46-56.

Bildstein, O., Trotignon, L., Perronnet, M., Jullien, M..2006. Modelling iron-clay interactions in deep geological disposal. Physics and Chemistry of the Earth 31, 618-625.

Bradbury, M.H., Baeyens, B.,1997. A mechanistic description of Ni and Zn sorption on Na-montmorillonite. Part II: Modelling. Journal of Contaminant Hydrology 27, 223-248.

Bradbury, M.H., Baeyens, B.,2005.) Modelling the sorption of Mn(II), Co(II), Ni(II), Zn(II), Cd(II), Eu(III), Am(III), Sn(IV), Th(IV), Np(V) and U(VI) on montmorillonite: Linear free energy relationships and estimates of surface binding constants for some selected heavy metals and actinides. Geochimica et Cosmochimica Acta 69, 875-892.

Dai, Z., Samper, J., Wolfsberg, A., Levitt, D., 2008. Identification of relative conductivity models for water flow and solute transport in unsaturated compacted bentonite. Physics and Chemistry of the Earth, Vol. 33, S177–S185. doi:10.1016/j.pce.2008.10.012.

De Windt, L., Pellegrini, D., Van der Lee, J., 2004. Coupled modeling of cement/claystone interactions and radionuclide migration. Journal of Contaminant Hydrology 68, 165-182.

ENRESA, 2004. Evaluación del comportamiento y de la seguridad de un lmacén geológico profundo de residuos radiactivos en arcilla. Informe ENRESA 49-1PP-M-A1-01 (In Spanish).

Fernández, A., Baeyens, B., Bradbury, M., Rivas, P., 2004. Analyses of the porewater chemical composition of a Spanish compacted bentonite used in a engineered barrier. Physics and Chemistry of the Earth 29, 105-118.

Fernández, A., Cuevas, J., Mäder, U.K., 2009a. Modelling concrete interaction with a bentonite barrier. European Journal of Mineralogy 21, 177-191.

Fernández, R., Mäder, U.K., Rodriguez, M., Vigil de la Villa, R., Cuevas, J., 2009b. Alteration of compacted bentonite by diffusion of highly alkaline solutions. European Journal of Mineralogy 21, 725–735.

Fritz, B., Madé, B., 1991. Geochemical modelling of bentonite-alkaline solutions interactions in the near-field of a repository for spent nuclear fuel. SKB Technical Report 91-05. Swedish Nuclear Fuel and Waste Management Company, Stockholm, Sweden.

Gaines, G.I.,Thomas, H.C. ,1953. Adsorption studies on clay minerals II. A formulation of the thermodynamics of exchange adsorption. Journal of Chemical Physics 21, 714–718.

Hayek, M., Kosakowski, G., Churakov, S., 2011, Exact analytical solutions for a diffusion problem coupled with a precipitation-dissolution reaction and feedback of porosity change, Water Resources Research, 47, W07545, doi:10.1029/2010WR010321.

Johnson, L., Gaus, I., Wieczorek, K., Mayor, J.-C., Sellin, P., Villar, M.-V., Samper, J., Cuevas, J.A., Gens, M., Velasco, M., Turrero, M.J., Montenegro, L., Martin, P.-L., Armand, G., 2014.

Integration of the Short-term Evolution of the Engineered Barrier System (EBS) with the Long-term Safety Perspective. PEBS Deliverable D4.1.

Kosakowski, G., Berner, U., 2013. The evolution of clay rock/cement interfaces in a cementitious repository for low- and intermediate level radioactive waste. Physics and Chemistry of the Earth 64, 65-86.

Lehikoinen, J., 2009. Bentonite-cement interaction -– Preliminary results from model calculations. Posiva Working Report WR 2009-37. Posiva Oy, Olkiluoto, Finland.

Lu, C., Samper, J., Fritz, B., Clement, A., Montenegro, L., 2011. Interactions of corrosion products and bentonite: An extended multicomponent reactive transport model. Physics and Chemistry of the Earth 36, 1661–1668, doi: 10.1016/j.pce.2011.07.013.

Marty, N.C.M., Tournassat, C., Burnol, A., Giffaut, E., Gaucher, E. C., 2009. Influence of reaction kinetics and mesh refinement on the numerical modelling of concrete/clay interactions. Journal of Hydrology 364, 58-72.

Marty, N.C.M, Fritz, B., Clément, A., Michau, N., 2010a. Modelling the long term alteration of the engineered bentonite barrier in an underground radioactive waste repository. Applied Clay Science 47, 82-90.

Marty, N., Claret, F., Gaboreau, S., Cochepin, B., Munier, I., Michau, N., Gaucher, E. C., Burnol, A., 2010b. Dual alteration of bentonite by iron corrosion and concrete interaction under high temperature conditions. In Clays in Natural and Engineered Barriers for Radioactive Waste Confinement, Nantes, France, pp. 473–474.

Molinero, J.,Samper, J., 2004. Groundwater Flow and Solute Transport in Fracture Zones: An Improved Model for a Large-Scale Field Experiment at Äspö (Sweden), Journal ofHydraulic Research. Vol. 42, Extra Issue, 157-172.

Montes-H,G., Marty, N., Fritz, B., Clement, A., Michau, N., 2005 Modelling of long-term diffusion-reaction in a bentonite barrier for radioactive waste confinement. Applied Clay Science, 30, 181-198.

Ngo, V. V., Delalande, M., Clément A., Michau, N., Fritz, B. ,2014. Coupled transport reaction modelling of the long-term interaction between iron, bentonite and Callovo-Oxfordian claystone in radioactive waste confinement systems. Applied Clay Science, 101, 430-443.

Samper, J., Juncosa, R., Delgado, J., Montenegro, L., 2000. CORE^{2D}: A code for non-isothermal water flow and reactive solute transport, Users manual version 2, Universidad de La Coruña, Publicación ENRESA, 131 pp.

Samper, J., Lu, C., Montenegro, L., 2008a. Coupled hydrogeochemical calculations of the interactions of corrosion products and bentonite. Physics and Chemistry of the Earth 33, S306–S316, doi:10.1016/j.pce.2008.10.009.

Samper J., Zheng, L., Montenegro, L., Fernández, A.M., Rivas, P., 2008b. Coupled thermo-hydro-chemical models of compacted bentonite after FEBEX in situ test, Applied Geochemistry, Vol 23/5: 1186-1201,

Samper, J., Xu, T.,Yang, C., 2009. A sequential partly iterative approach for multicomponent reactive transport with CORE^{2D}. Computational Geosciences. doi: 10.1007/s10596-008-9119-5.

Samper, J, Yang, C., Zheng, L., Montenegro, L., Xu, T., Dai, Z., Zhang, G., Lu, C.,Moreira, S., 2011. CORE^{2D} V4: A code for water flow, heat and solute transport, geochemical reactions, and microbial processes, Chapter 7 of the Electronic book *Groundwater Reactive Transport Models*, F Zhang, G-T Yeh, C Parker & X Shi (Ed), Bentham Science Publishers, pp 161-186, ISBN 978-1-60805-029-1.

Samper, J., Naves, A., Montenegro, L., Mon., A., 2016. Reactive transport modelling of the long-term interactions of corrosion products and compacted bentonite in a HLW repository in granite: Uncertainties and relevance for performance assessment, Applied Geochemistry. Vol 67 (2016) 42-51.

Sánchez, L., Cuevas, J., Ramírez S., Riuiz De León, D., Fernández, R., Vigil Dela Villa, R., Leguey S. ,2006. Reaction kinetics of FEBEX bentonite in hyperalkaline conditions resembling the cement-bentonite interface. Applied Clay Science, 33, 125-141.

Savage, D., 2011. A review of analogues of alkaline alteration with regard to long-term barrier performance. Mineralogical Magazine 75, 2401–2418.

Savage, D., 2012. Prospects for coupled modelling. STUK-TR 13. Radiation and Nuclear Safety Authority.

Savage, D., Bateman, K., Hill, P., Hughes, C., Milodowski, A., Pearce, J., Rae, E., Rochelle, C., 1992. Rate and mechanism of the reaction of silicates with cement pore fluids. Applied Clay Science 7, 33-45.

Savage, D., Noy, D. J., Mihara, M., 2002. Modelling the interaction of bentonite with hyperalkaline fluids. Applied Geochemistry 17, 207-223.

Savage, D., Watson, C., Benbow, S., Wilson, J., 2010a. Modelling iron/bentonite interactions. Applied Clay Science 47, 91-98.

Savage, D., Benbow, S., Watson, C., Takase, H., Ono, K., Oda, C., Honda, A., 2010b. Natural systems evidence for the alteration of clay under alkaline conditions: an example from Searles Lake, California. Applied Clay Science 47, 72–81.

Savage, D., Arthur, R., Watson, C., Wilson, J., 2010c. An evaluation of models of bentonite pore water evolution. SSM Technical Report 2010:12. Swedish Radiation Safety Authority, Stockholm, Sweden.

Savage, D., Soler, J.M., Yamaguchi, K., Walker, C., Honda, A., Inagaki, M., Watson, C., Wilson, J., Benbow, S., Gaus, I., Rueedi, J., 2011. A comparative study of the modelling of cement hydration and cement-rock laboratory experiments. Applied Geochemistry 26, 11381152.

Shao, H., Kosakowski, G., Berner, U., Kulik, D.A., Mäder, U., Kolditz, O., 2013. Reactive transport modeling of the clogging process at Maqarin natural analogue site. Physics and Chemistry of the Earth 64, 21-31.

Soler, J.M., Paris, B., Pfingsten, W., Mäder, U., 2004. Flow and reactive transport modeling in the framework of GTS-HPF. Water–Rock Interaction XI. Balkema, Rotterdam, The Netherlands, pp. 983–987.

Soler J.M, Samper, J., Yllera, A., Hernández, A., Quejido, A., Fernández, M., Yang, C., Naves, A., P. Hernán, and P. Wersin, 2008. The DI-B in-situ diffusion experiment at mont terri: results and modelling, Physics and Chemistry of the Earth, Vol. 33. Supplement 1, 2008, S196-S207.

Steefel, C.I., Lichtner, P.C., 1998. Multicomponent reactive transport in discrete fractures II. Infiltration of hyperalkaline groundwater at Maqarin, Jordan, a natural analogue site. Journal of Hydrology 209, 200-224.

Tinseau, E., Bartier, D., Hassouta, L., Devol-Brown, I., Stammose, D., 2006. Mineralogical characterization of the Tournemire argillite after in situ reaction with concretes. Wate Management 26, 789-800.

Tournassat, C., 2003. Cations-clay interactions: The Fe(II) case. Application to the problematic of the French deep nuclear repository field concept. Ph.D. Dissert. Grenoble, France.

Ueda, H., Hyodo, H., Takase, H., Savage, D., Benbow, S., Noda, M., 2007. Evaluation of the kinetics of cement-bentonite interaction in a HLW repository using the reactive solute transport simulator. In 15th International Conference on Nuclear Engineering, Nagoya, Japan, pp. ICONE15-10566.

Watson, C., Benbow, S., Savage, D., 2007. Modelling the interaction of low pH cements and bentonite. Issues affecting the geochemical evolution of repositories for radioactive waste. SKI Report 2007:30. Swedish Nuclear Power Inspectorate, Stockholm, Sweden..

Watson, C., Hane, K., Savage, D., Benbow, S., Cuevas, J., Fernández, R., 2009a. Reaction and diffusion of cementitious water in bentonite: results of 'blind' modelling. Applied Clay Science 45, 54–69.

Watson, C., Hane, K., Savage, D., Benbow, S., Cuevas, J., Fernández, R., Norris, S., Amme, M., 2009b. Modelling diffusion and reaction of cementitious water in bentonite. In The Scientific Basis for Nuclear Waste Management XXXIII, 413–420. Burakov and A.S. Aloy, Eds.

Watson, C., Savage, D., Wilson, J., Benbow, S., Walker, C., Norris, S., 2013. The Tournemire industrial analogue: reactive transport modelling of a cement-clay interface. Clay Minerals 48, 167-184.

Watson, C., Wilson, J., Savage, D., Benbow, S., Norris, S., 2016. Modelling reactions between alkaline fluids and fractured rock: The Maqarin natural analogue. Applied Clay Science 121-122, 46–56.

Wersin, P., Birgersson, M., Olsson, S., Karnland, O., Snellman, M., 2007. Impact of corrosion-derived iron on the bentonite buffer within the KBS-3H disposal concept – The Olkiluoto site as case study. Posiva Report 2007/11. Posiva Oy, Olkiluoto, Finland.

Wolery, T.J., 1992. EQ3/6, a software package for geochemical modeling of aqueous systems: Package overview and installation guide (version 7.0). Technical Report UCRL-MA-110662-Pt 1. Lawrence Livermore National Laboratory, CA, USA.

Xu, T., Samper, J., Ayora, C., Manzano, M.,Custodio, E., 1999. Modeling of non iso-thermal multicomponent reactive transport in field scale porous media flow systems. Journal of Hydrology 214, 144–164.

Yamaguchi, T., Sakamoto, Y., Akai, M., Takazawa, M., Iida, Y., Tanaka, T., Nakayama, S., 2007. Experimental and modeling study on long-term alteration of compacted bentonite with alkaline groundwater. Physics and Chemistry of the Earth 32, 298-310.

Yang, C., Samper, J., Montenegro, L., 2008a. A coupled non-isothermal reactive transport model for long-term geochemical evolution of a HLW repository in clay. Environmental Geology 53, 1627–1638, doi: 10.1007/s00254-007-0770-2.

Yang, C, Samper, J., Molinero, J., 2008b. Inverse microbial and geochemical reactive transport models in porous media, Physics and Chemistry of the Earth, Vol. 33 Issues 12-13: 1026-1034.

Yang, C., Romanak, K., Hovorka, S., Triveno, R., 2013. Modeling CO_2 Release Experiment in the Shallow Subsurface and Sensitivity Analysis, Environmental & Engineering Geoscience, v. 19 no. 3 p. 207-220.

Yang, C., Hovorka, S. D., Treviño, R. H., Delgado-Alonso, J. ,2015. Integrated Framework for Assessing Impacts of CO_2 Leakage on Groundwater Quality and Monitoring-Network Efficiency: Case Study at a CO_2 Enhanced Oil Recovery Site, Environmental Science and Technology, 2015, 49 (14), 8887–8898.

Zhang, G., Samper, J., Montenegro, L., 2008. Coupled thermo-hydro-bio-geochemical reactive transport model of the CERBERUS heating and radiation experiment in Boom clay, Applied Geochemistry, Vol 23/4: 932-949.

Zheng, L., Samper, J., 2008. Coupled THMC model of FEBEX mock-up test. Physics and Chemistry of the Earth 33, S486–S498, doi:10.1016/j.pce.2008.10.023.

Zheng, L., Samper, J., Montenegro, L., Fernández, AM., 2010. A coupled THMC model of a heating and hydration laboratory experiment in unsaturated compacted FEBEX bentonite. Journal of Hydrology 386, 80-94, doi: 10.1016/j.jhydrol.2010.03.009.

Zheng, L., Samper, J., Montenegro, L., 2011. A coupled THC model of the FEBEX in situ test with bentonite swelling and chemical and thermal osmosis. Journal of Contaminant Hydrology 126, 45-60.

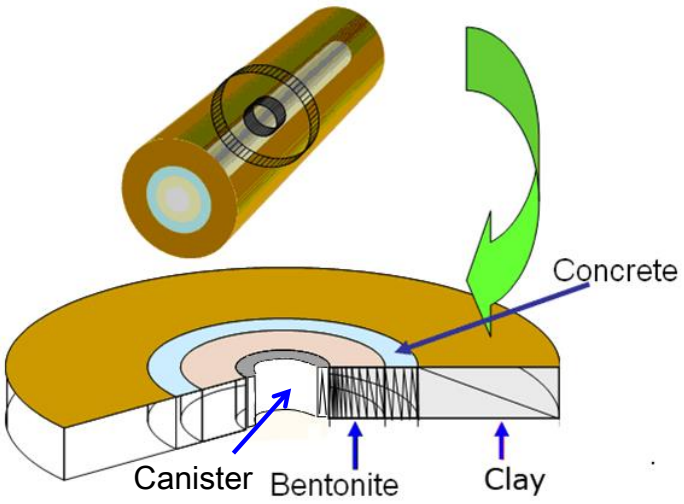

Fig. 1. Scheme of the multibarrier system of a HLW repository in clay according to the Spanish Reference Concept (Yang *et al.*, 2008a).

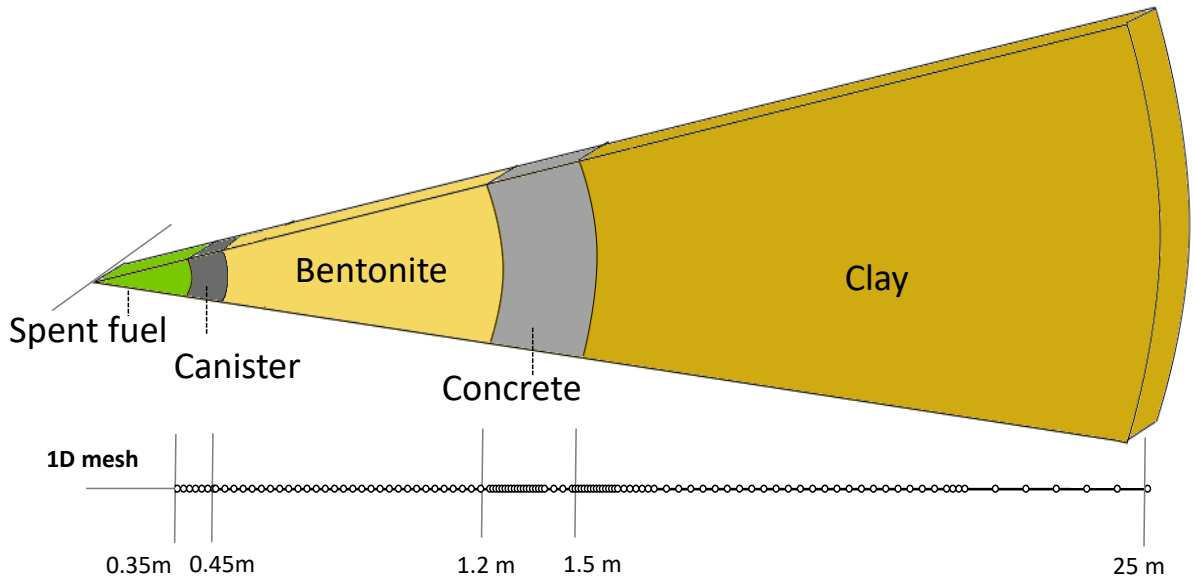

Fig. 2. 1-D finite element grid which accounts for the canister, the bentonite barrier, the concrete liner and the clay formation.

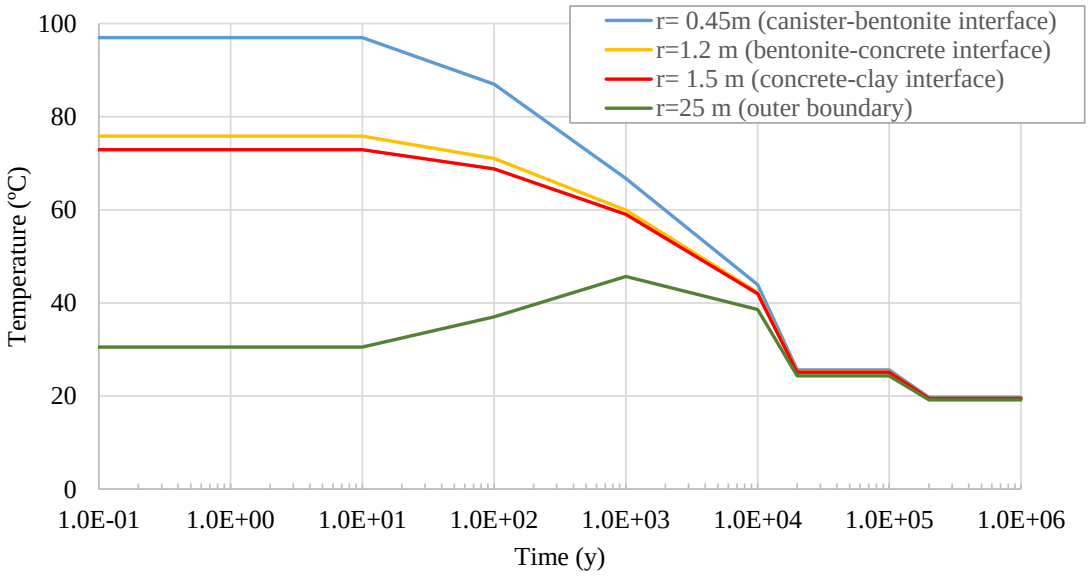

Fig 3. Time evolution of the temperatures prescribed at the canister-bentonite interface (r = 0.45 m), the bentonite-concrete interface (r = 1.2 m), the concrete-clay interface (r = 1.5 m) and the outer boundary (r = 25 m).

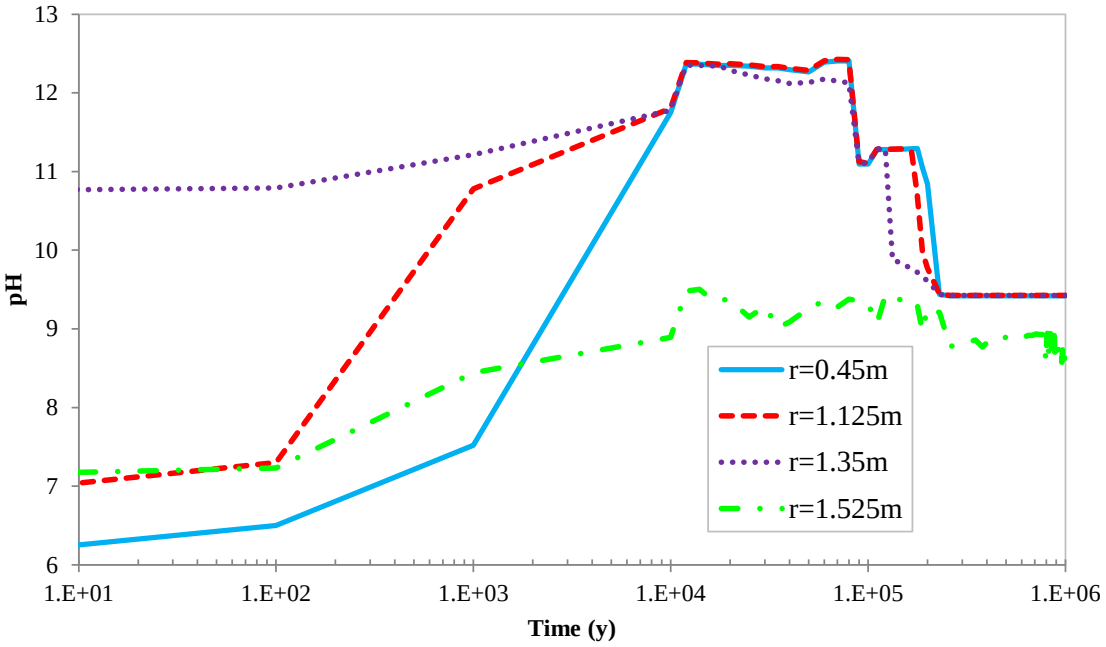

Fig. 4 Time evolution of the computed pH at the canister-bentonite interface (r = 0.45 m), the bentonite near the concrete interface (r = 1.125 m), the concrete midpoint (r = 1.35 m) and the clay near the concrete interface (r = 1.525 m).

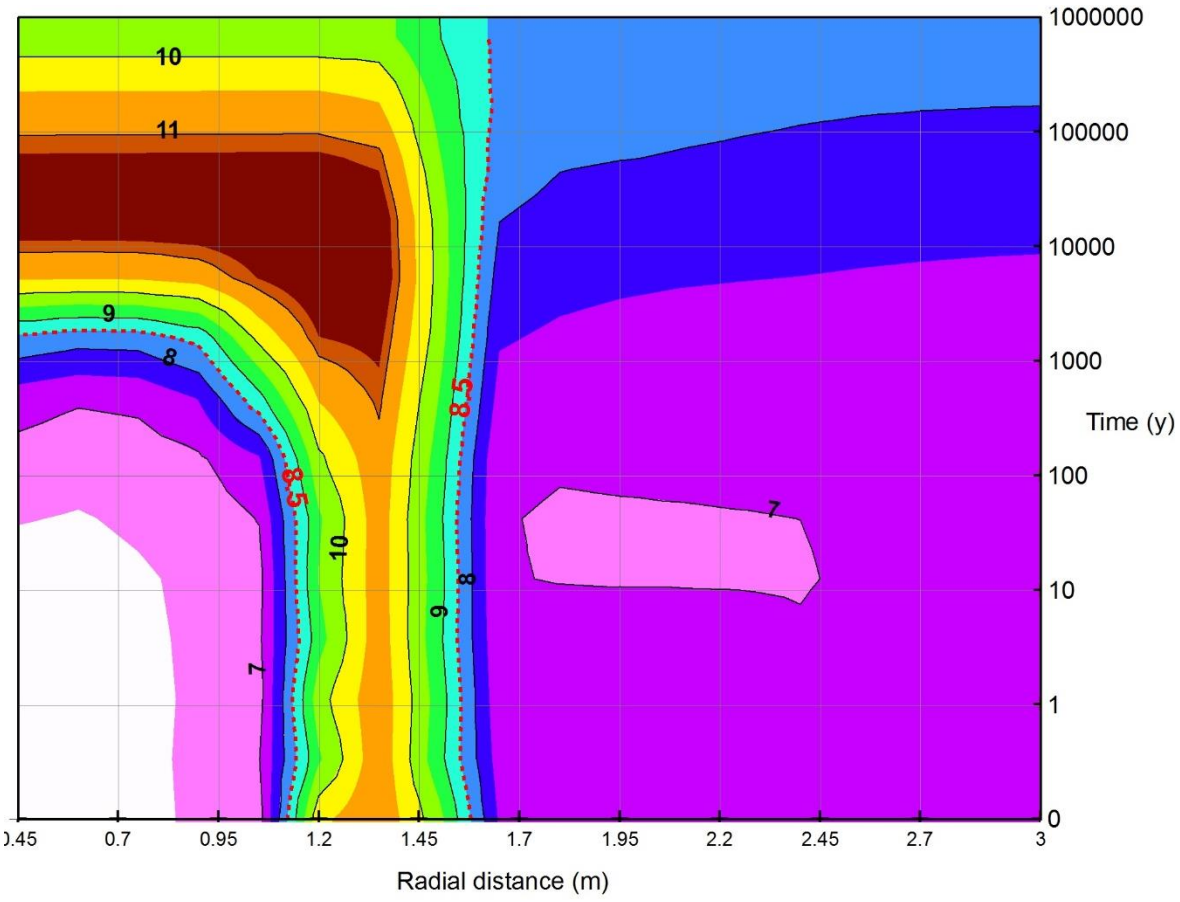

Fig. 5 Contour plot of computed pH as a function of radial distance and time.

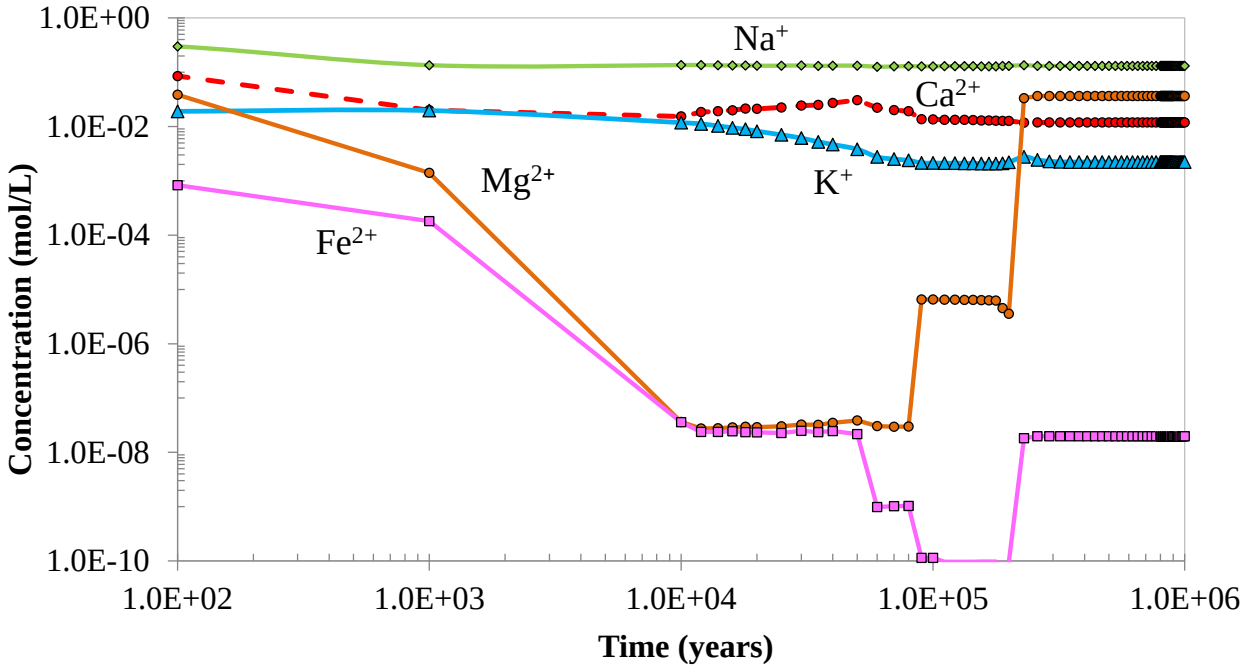

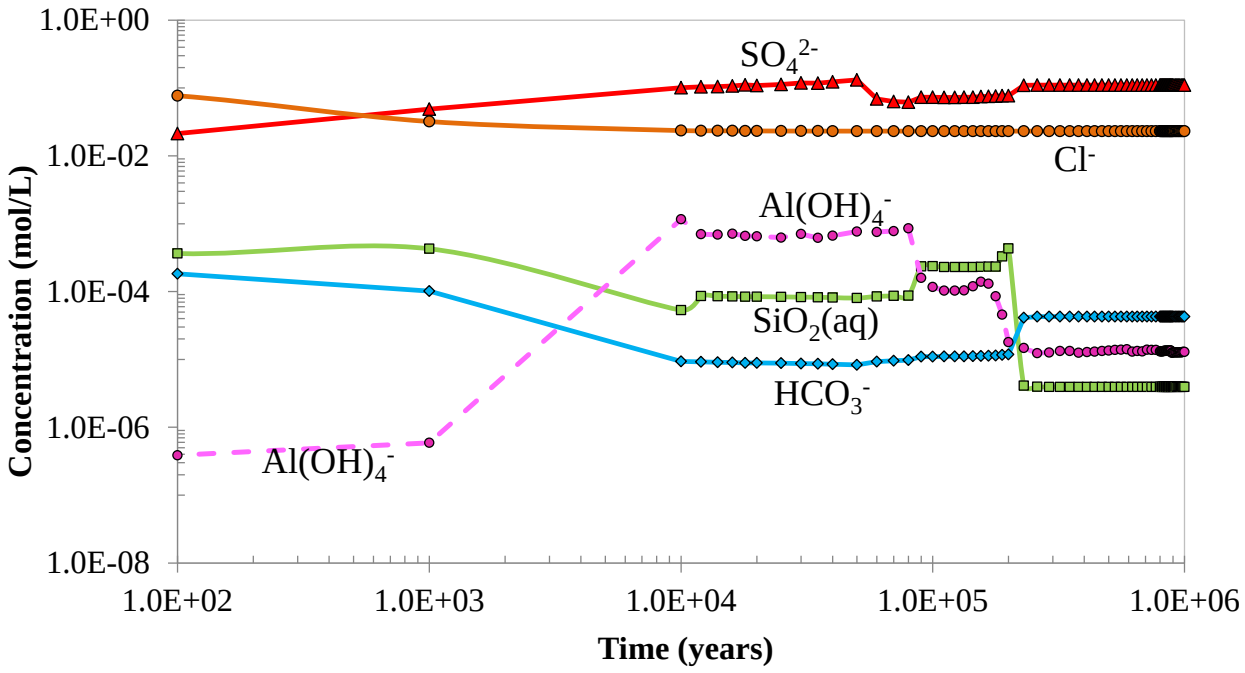

Fig. 6 Time evolution of the computed concentrations of dissolved Na^{+}, Ca^{2+}, K^{+}, Mg^{2+}, Fe^{2+} (top) and SO_4^{2-}, Cl^{-}, $SiO_2(aq)$, HCO_3^{-} and $Al(OH)_4^{-}$ (bottom) at the canister-bentonite interface (r = 0.45 m).

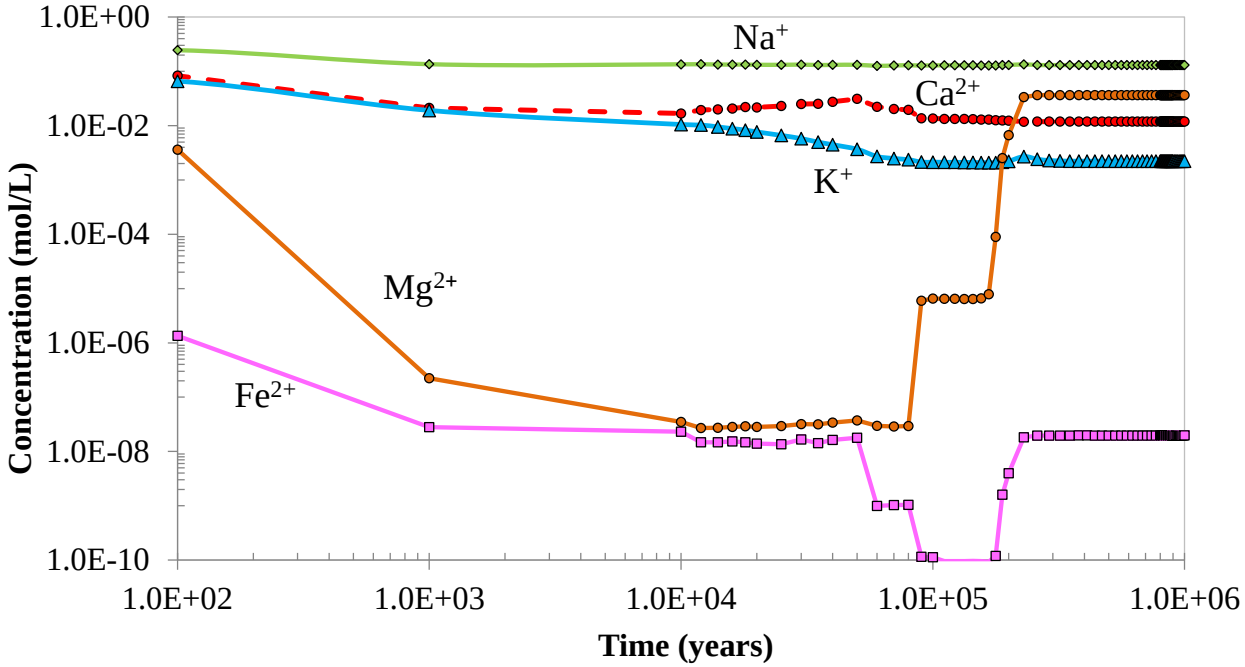

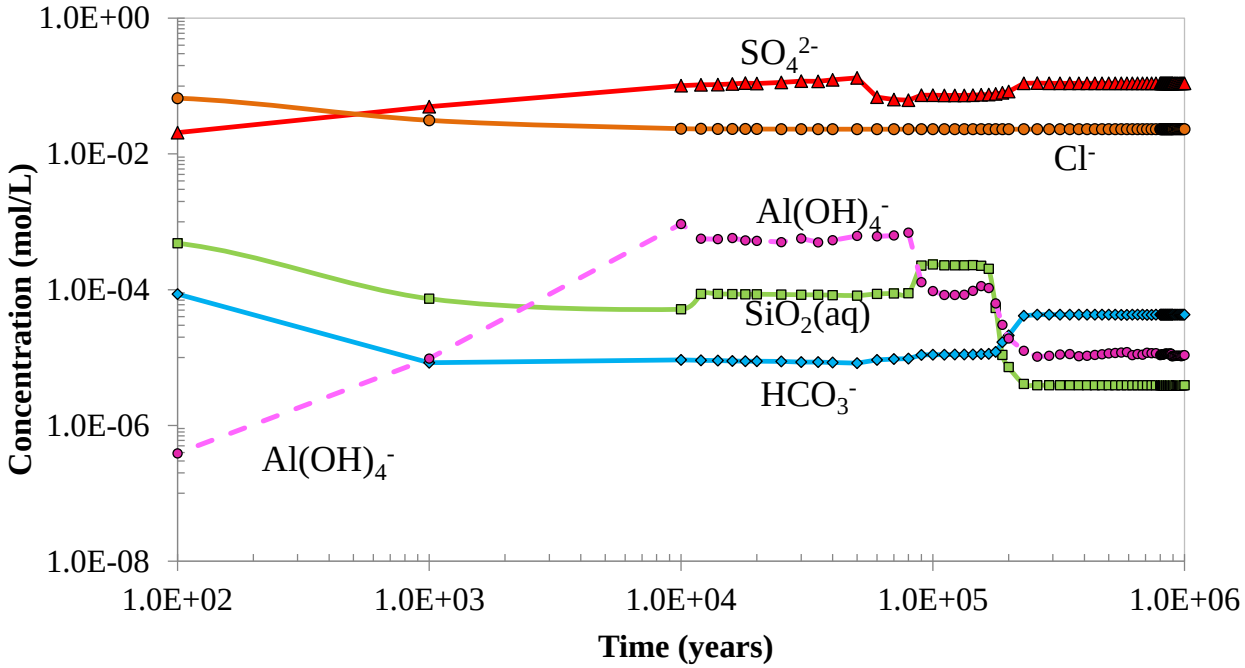

Fig. 7 Time evolution of the computed concentrations of the dissolved Na^+, Ca^{2+}, K^+, Mg^{2+}, Fe^{2+} (top) and SO_4^{2-}, Cl^-, $SiO_2(aq)$, HCO_3^- and $Al(OH)_4^-$ (bottom) in the bentonite near the concrete interface (r = 1.125 m).

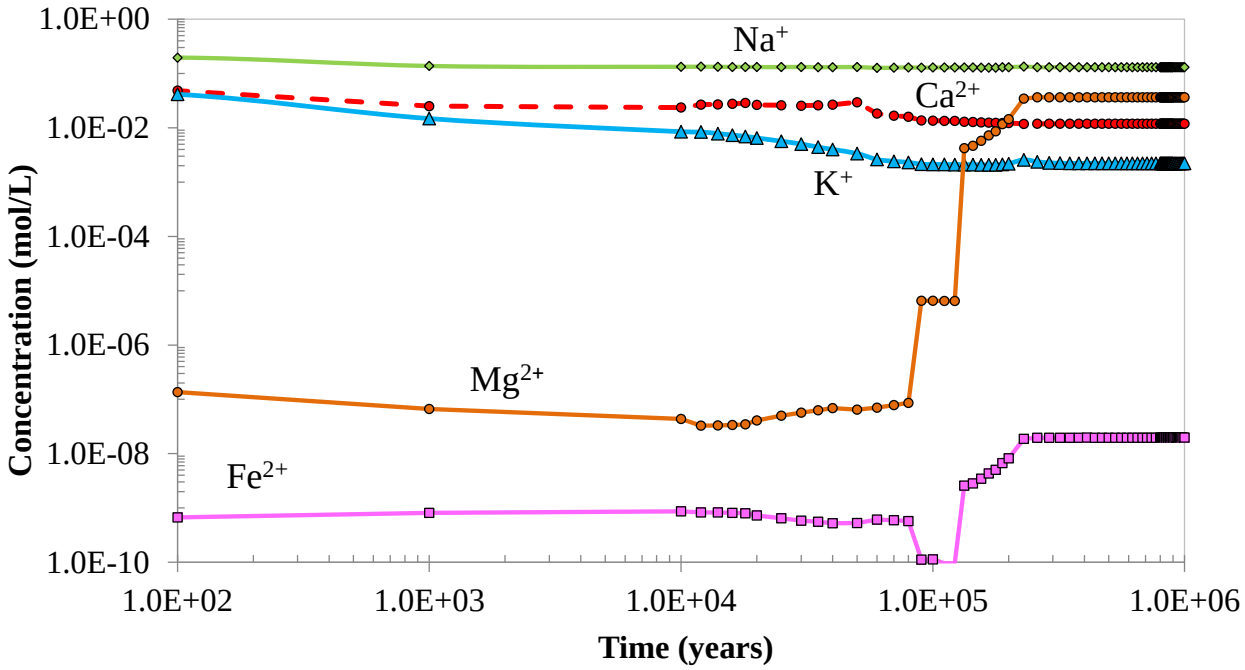

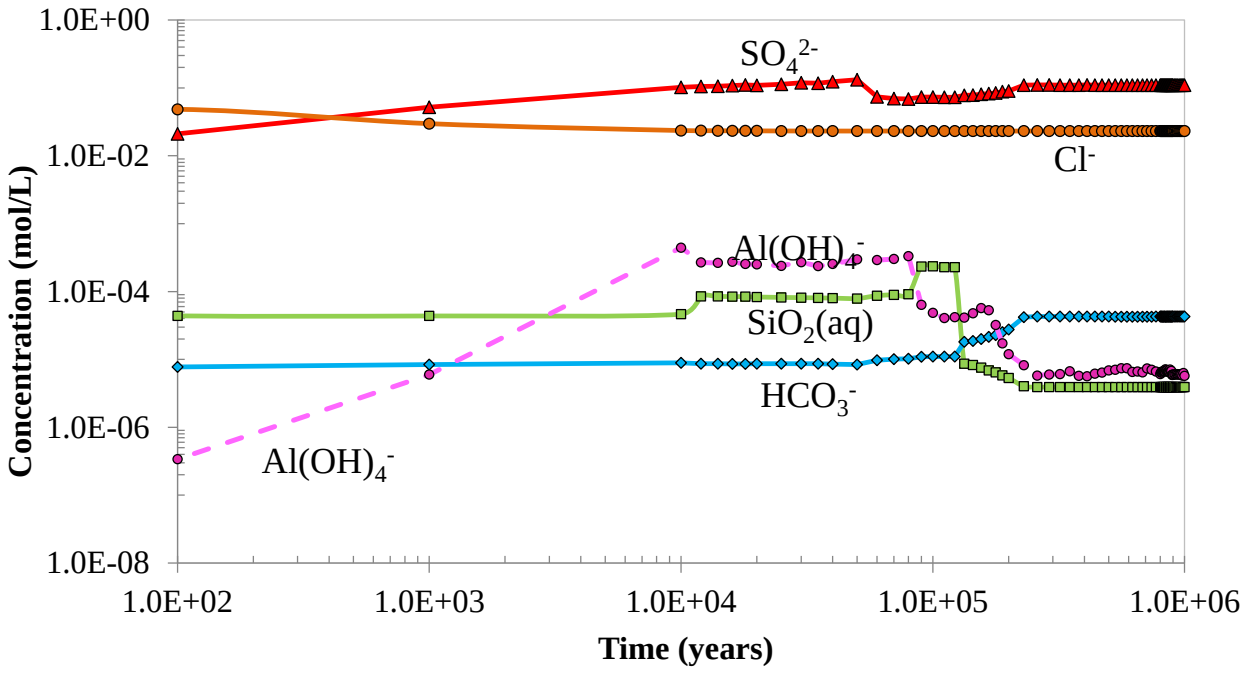

Fig. 8. Time evolution of the computed concentrations of the dissolved Na^{+}, Ca^{2+}, K^{+}, Mg^{2+}, Fe^{2+} (top) and SO_4^{2-}, Cl, SiO_2(aq), HCO_3^{-} and $Al(OH)_4^{-}$ (bottom) in the midpoint of the concrete liner (r = 1.35 m).

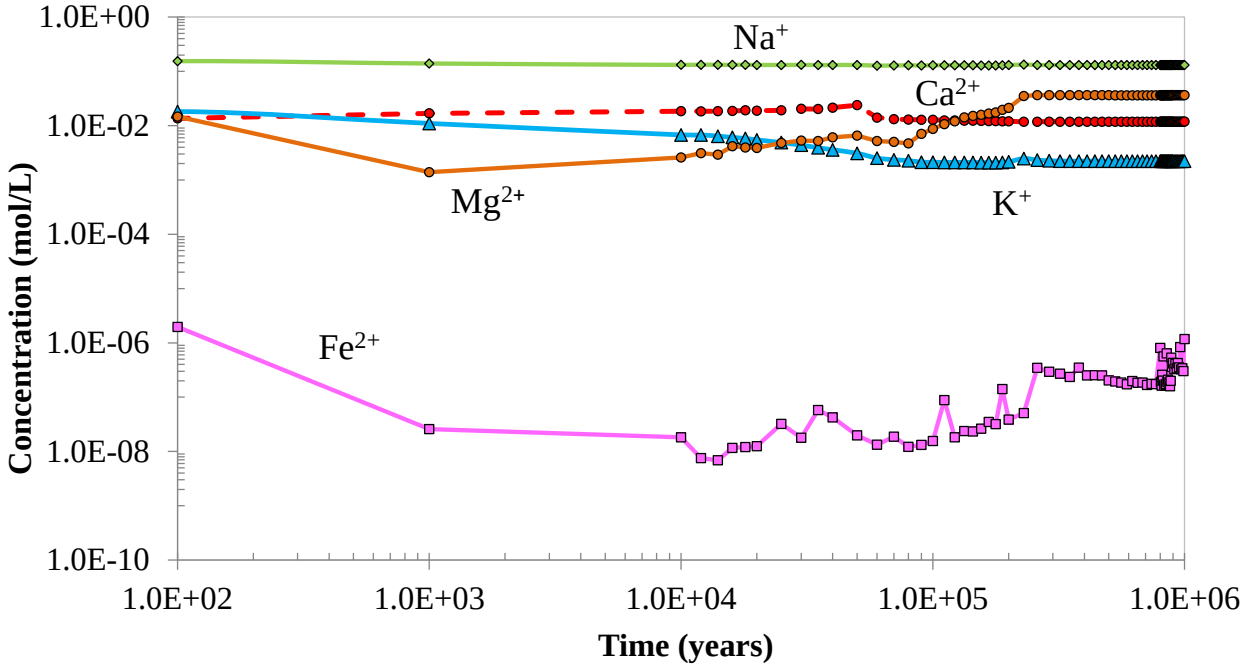

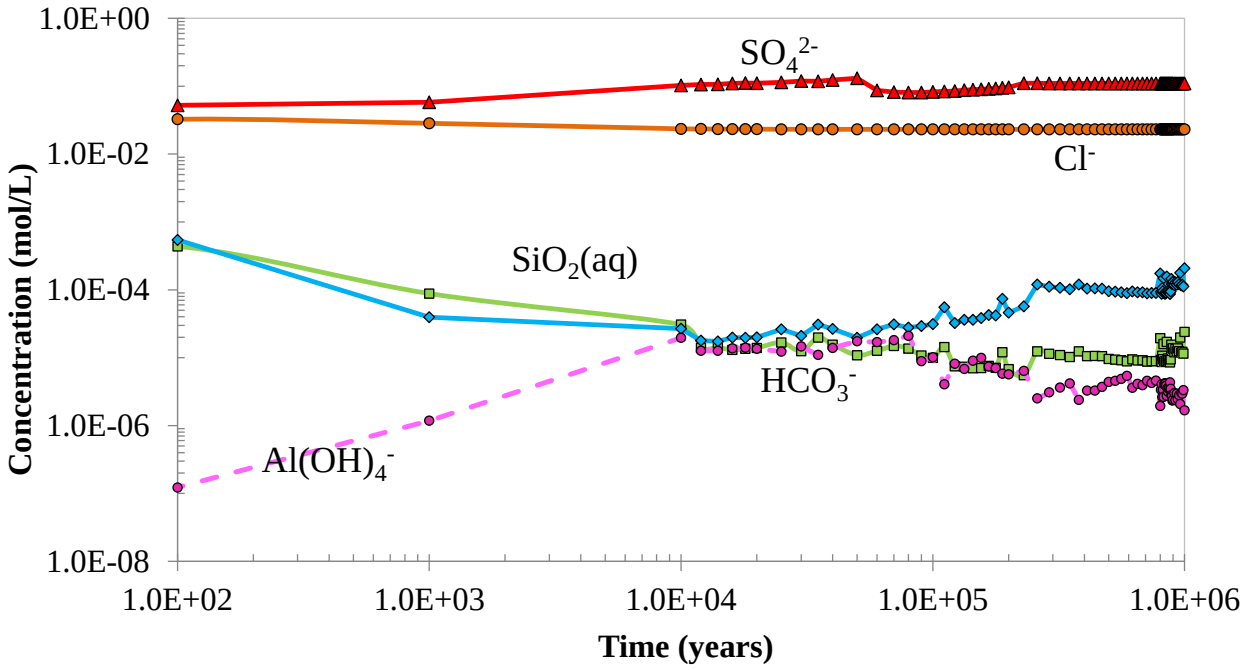

Fig. 9. Time evolution of the computed concentrations of the dissolved Na^+, Ca^{2+}, K^+, Mg^{2+}, Fe^{2+} (top) and SO_4^{2-}, Cl^-, $SiO_2(aq)$, HCO_3^- and $Al(OH)_4^-$ (bottom) in the clay formation near the concrete interface (r = 1.525 m).

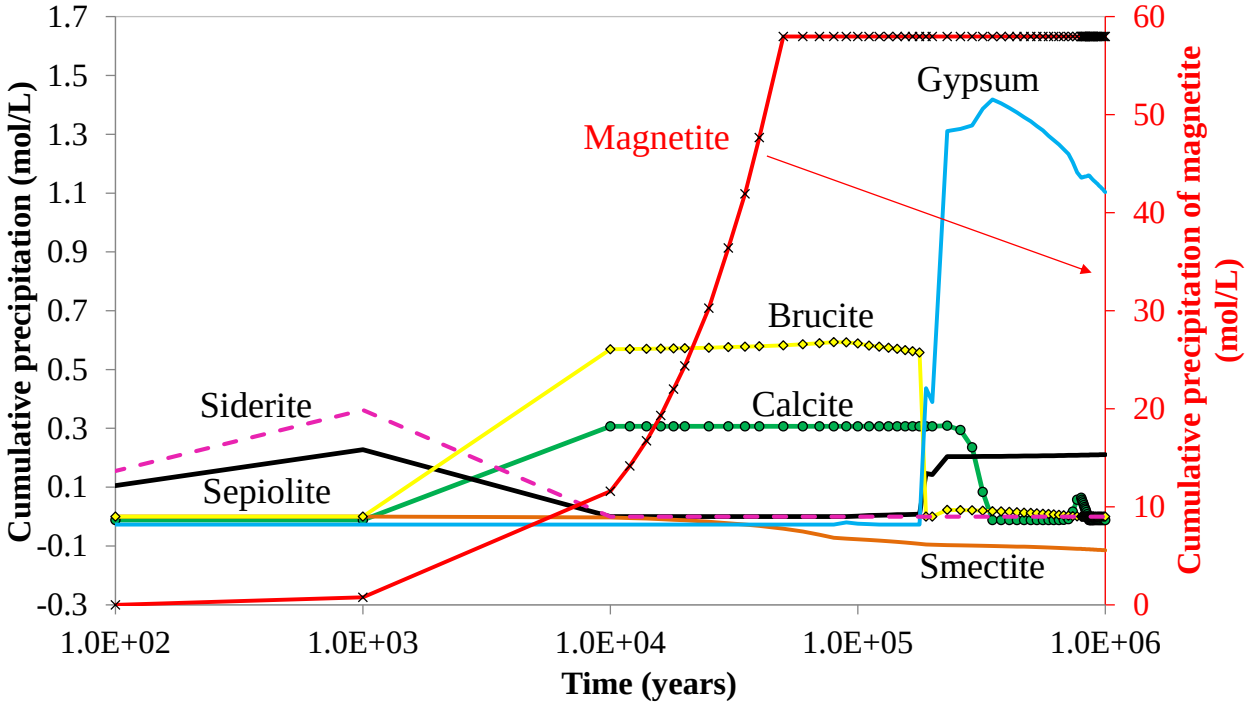

Fig. 10. Time evolution of the computed cumulative mineral dissolution/precipitation at the canister-bentonite interface (r = 0.45 m) (positive for precipitation and negative for dissolution).

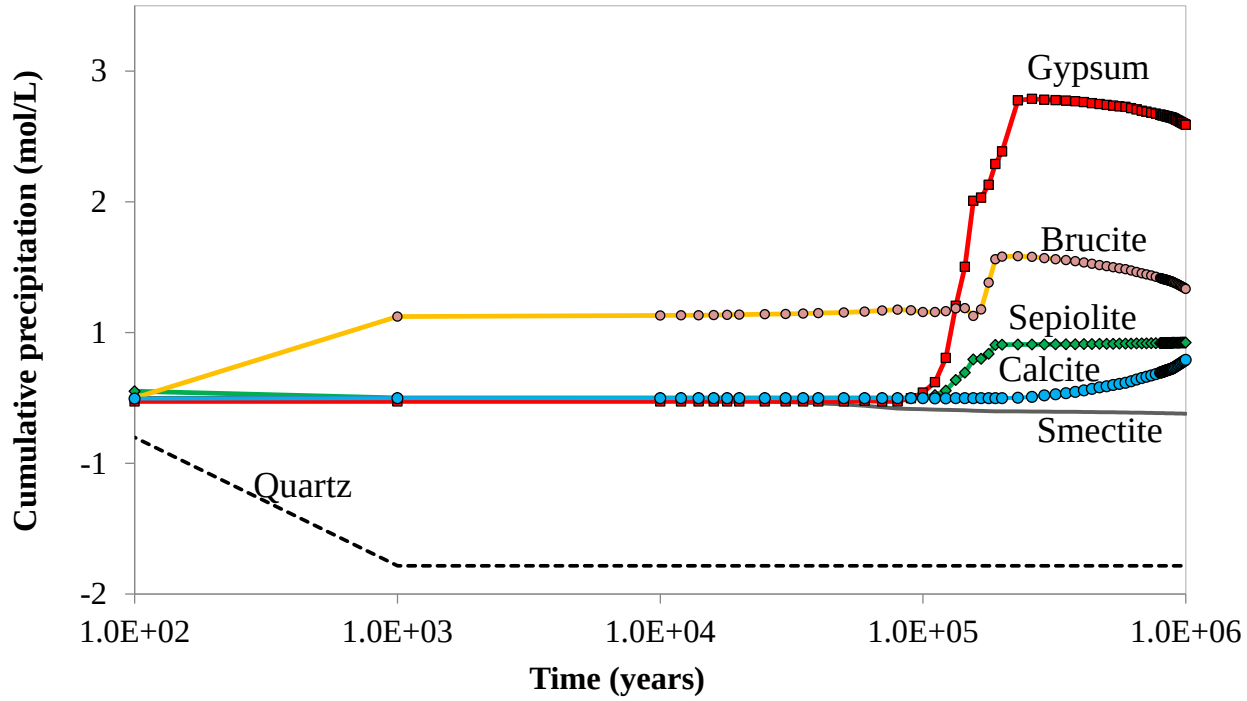

Fig. 11. Time evolution of the computed cumulative mineral dissolution/precipitation in the bentonite buffer near the concrete interface (r = 1.125 m) (positive for precipitation and negative for dissolution).

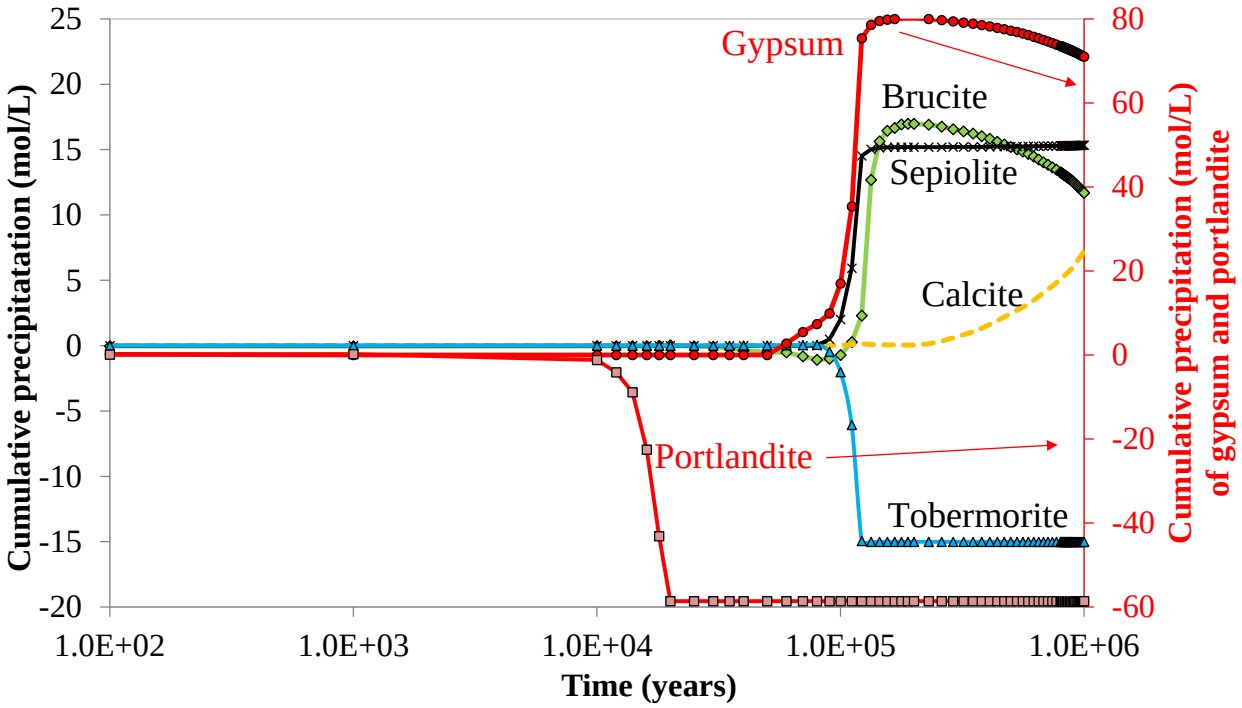

Fig. 12. Time evolution of the computed cumulative mineral dissolution/precipitation at the midpoint of the concrete liner (r = 1.35 m) (positive for precipitation and negative for dissolution).

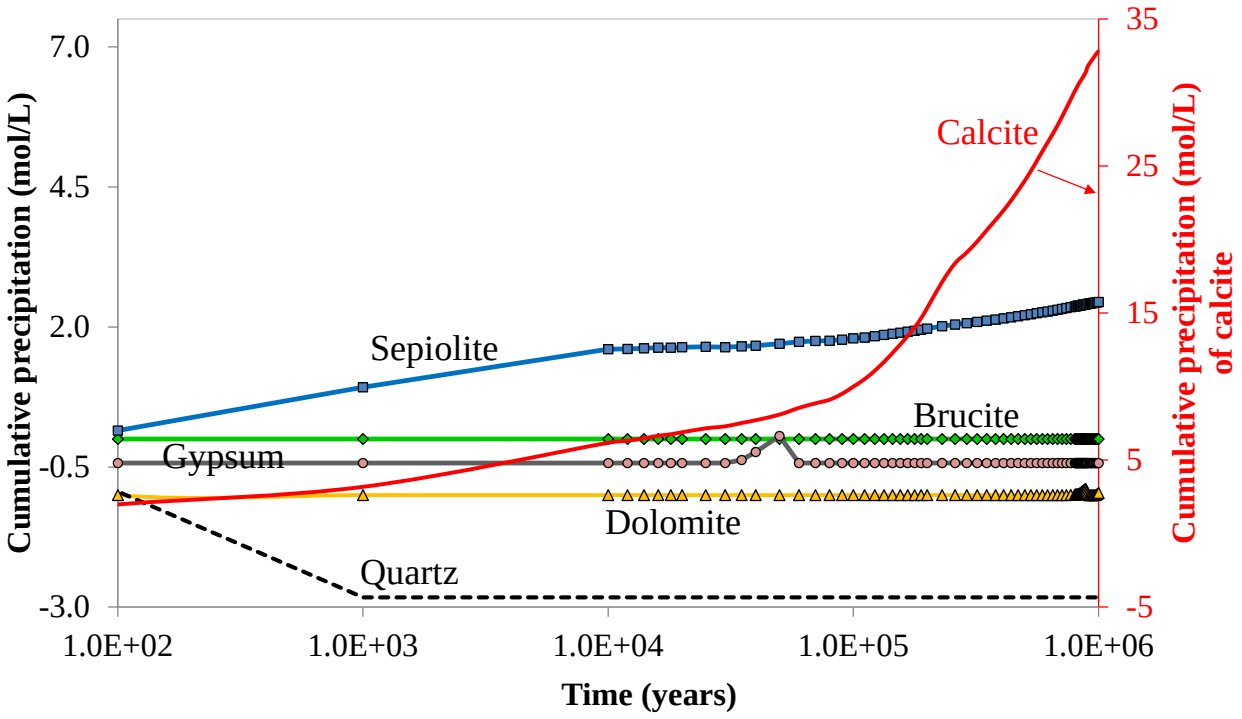

Fig. 13. Time evolution of the computed cumulative mineral dissolution/precipitation in the clay formation near the concrete interface (r = 1.525 m) (positive for precipitation and negative for dissolution).

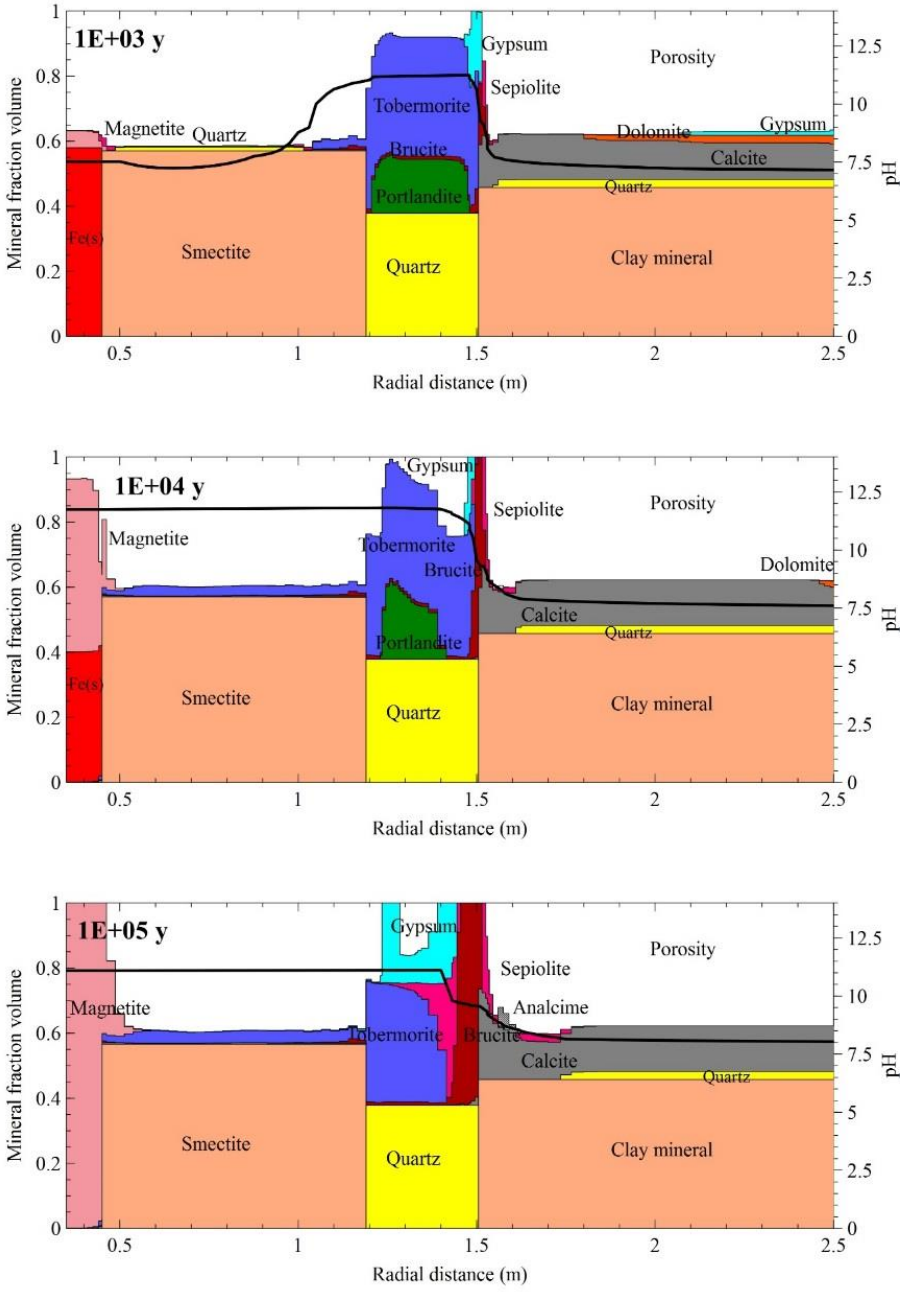

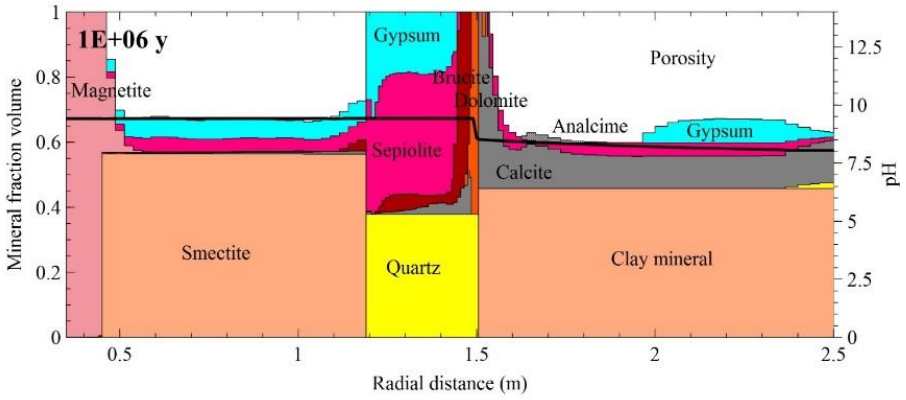

Fig. 14. Computed pH and mineral volume fractions at selected times.

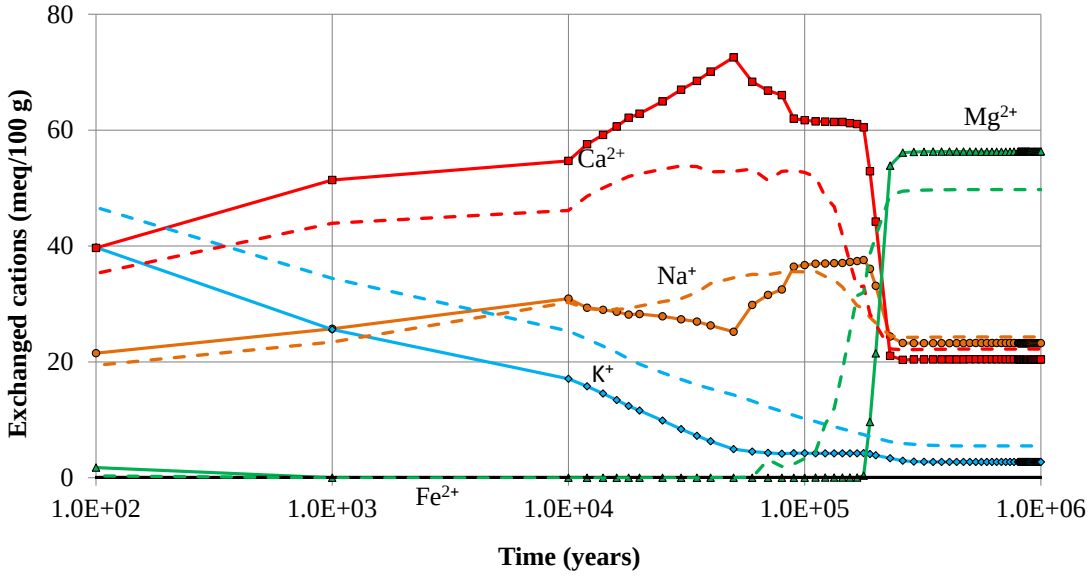

Fig. 15 Time evolution of the computed concentrations of exchanged cations in the bentonite near the concrete interface (r = 1.125 m) in the base run (thick lines) and the sensitivity run to changes in the selectivity coefficients (dashed lines).

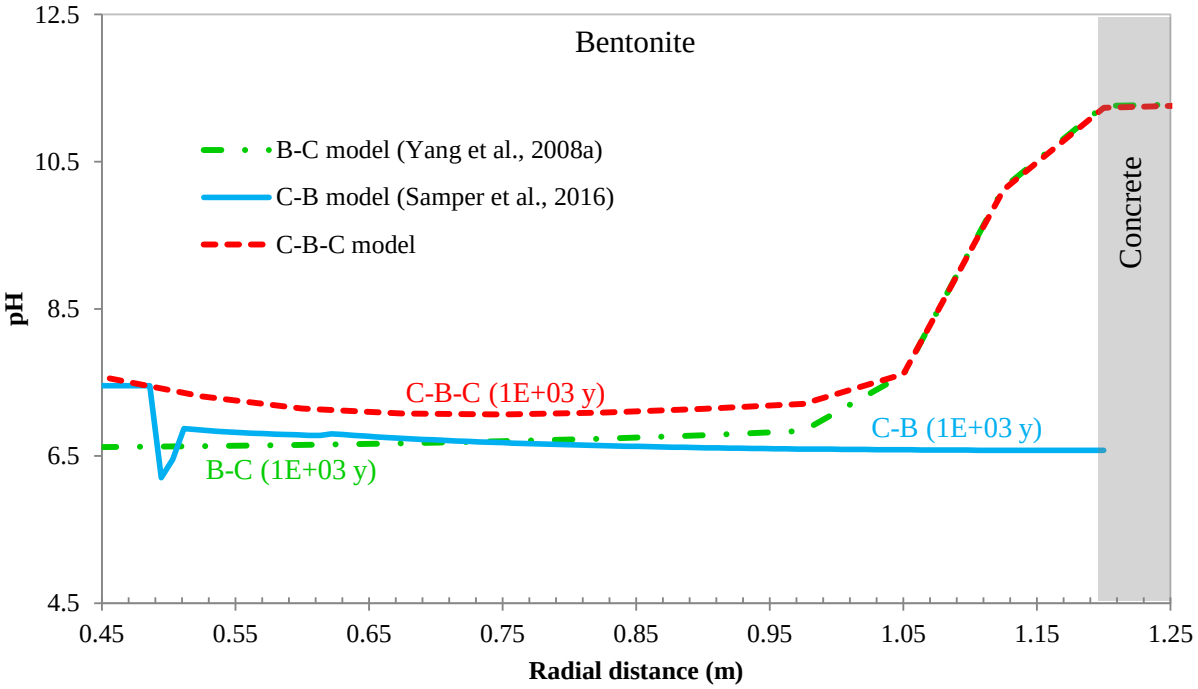

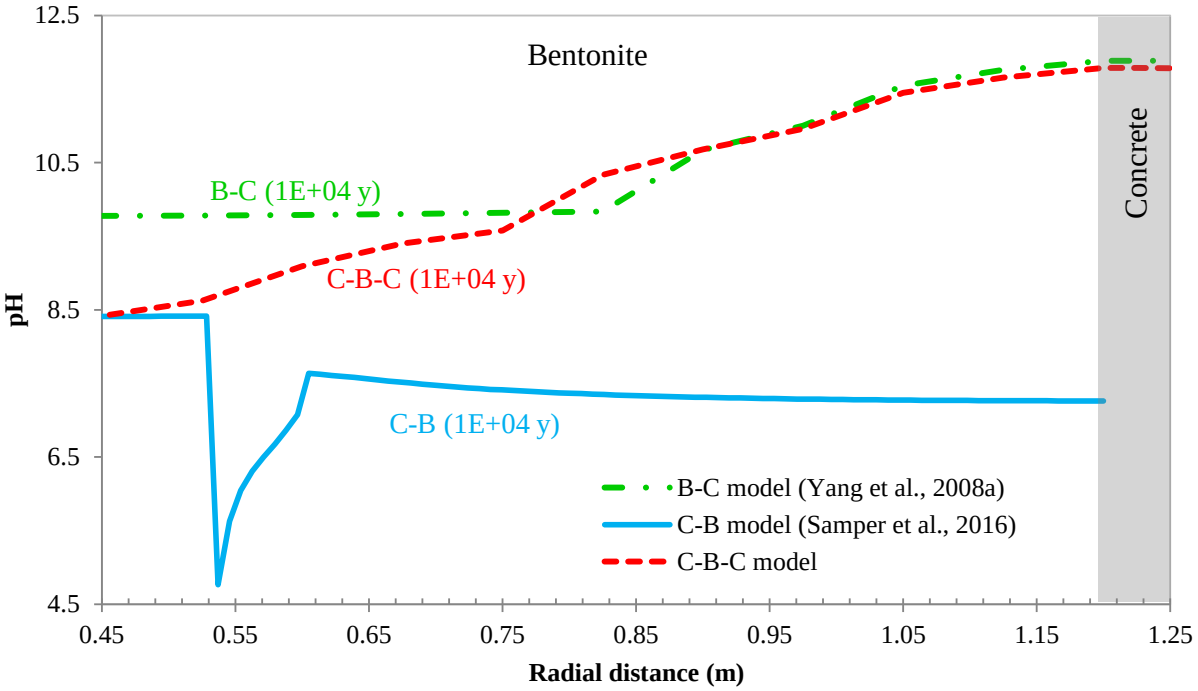

Fig. 16 Radial distribution of the computed pH at 10^3 years (top) and 10^4 years (bottom) with: 1) A model with canister corrosion, bentonite and concrete degradation (C-B-C model), 2) A model with canister corrosion and bentonite, but no concrete degradation (C-B model), and 3) A model without canister corrosion (B-C model).

Table 1. Reactions and equilibrium constants for aqueous species and mineral dissolution/precipitation at 25ºC (Wolery, 1992); protolysis constants for surface complexation reactions for a triple-site sorption model (Bradbury & Bayens, 2005); and the selectivity constants for cation exchange reactions. The selectivities within parentheses are those of the sensitivity run and were derived from Yang *et al.* (2008a).

Aqueous complexes	LogK (25ºC)
$OH^- + H^+ \Leftrightarrow H_2O$	13.9951
$CO_3^{2-} + H^+ \Leftrightarrow HCO_3^-$	10.3288
$CaCO_3(aq) + H^+ \Leftrightarrow Ca^{2+} + HCO_3^-$	7.0017
$CaHCO_3^+ \Leftrightarrow Ca^{2+} + HCO_3^-$	-1.0467
$CaSO_4(aq) \Leftrightarrow Ca^{2+} + SO_4^{2-}$	-2.111
$CaOH^+ + H^+ \Leftrightarrow Ca^{2+} + H_2O$	12.850
$CaCl^- \Leftrightarrow Ca^{2+} + Cl^-$	0.6956
$CaCl_2(aq) \Leftrightarrow Ca^{2+} + 2Cl^-$	0.6436
$Ca(H_3SiO_4)_2(aq) + 2H^+ \Leftrightarrow Ca^{2+} + 2SiO_2(aq) + 4H_2O$	15.053
$CaH_2SiO_4(aq) + 2H^+ \Leftrightarrow Ca^{2+} + SiO_2(aq) + 2H_2O$	18.561
$CaH_3SiO_4^+ + H^+ \Leftrightarrow Ca^{2+} + SiO_2(aq) + 2H_2O$	8.7916
$MgCO_3(aq) \Leftrightarrow Mg^{2+} + CO_3^{-2}$	-2.9789
$MgHCO_3^+ \Leftrightarrow Mg^{2+} + HCO_3^-$	-1.0357
$MgSO_4(aq) \Leftrightarrow Mg^{2+} + SO_4^{2-}$	-2.4117
$MgCl^+ \Leftrightarrow Mg^{2+} + Cl^-$	0.1349
$MgOH^+ + H^+ \Leftrightarrow Mg^{2+} + H_2O$	11.607
$Mg_4(OH)_4^{4+} + 4H^+ \Leftrightarrow 4Mg^{2+} + 4H_2O$	39.750
$MgH_2SiO_4(aq) + 2H^+ \Leftrightarrow Mg^{2+} + SiO_2(aq) + 2H_2O$	17.4816
$MgH_3SiO_4^+ + H^+ \Leftrightarrow Mg^{2+} + SiO_2(aq) + 2H_2O$	8.5416
$Mg(H_3SiO_4)_2(aq) + 2H^+ \Leftrightarrow Mg^{2+} + 2SiO_2(aq) + 4H_2O$	13.723
$NaOH(aq) + H^+ \Leftrightarrow Na^+ + H_2O$	14.180
$NaCl(aq) \Leftrightarrow Na^+ + Cl^-$	0.777
$NaCO_3^- + H^+ \Leftrightarrow Na^+ + HCO_3^-$	9.836
$NaHCO_3(aq) \Leftrightarrow Na^+ + HCO_3^-$	-0.1541
$NaHSiO_3(aq) + H^+ \Leftrightarrow H_2O + Na^+ + SiO_2(aq)$	8.6616
$CO_2(aq) + H_2O \Leftrightarrow H^+ + HCO_3^-$	-6.3447
$KOH(aq) + H^+ \Leftrightarrow K^+ + H_2O$	14.460
$KCl(aq) \Leftrightarrow K^+ + Cl^-$	1.4946
$KSO_4^- \Leftrightarrow K^+ + SO_4^{2-}$	-0.8796
$KHSO_4(aq) \Leftrightarrow H^+ + K^+ + SO_4^{2-}$	-0.8136
$NaSO_4^- \Leftrightarrow Na^+ + SO_4^{2-}$	-0.8200
$NaH_3SiO_4(aq) + H^+ \Leftrightarrow 2H_2O + Na^+ + SiO_2(aq)$	8.6616
$H_3SiO_4^- + H^+ \Leftrightarrow SiO_2(aq) + 2H_2O$	9.8120
$H_2SiO_4^{2-} + 2H^+ \Leftrightarrow 2H_2O + SiO_2(aq)$	22.9116
$HSiO_3^- + H^+ \Leftrightarrow H_2O + SiO_2(aq)$	9.9525
$H_4(H_2SiO_4)_4^{4-} + 4H^+ \Leftrightarrow 8H_2O + 4SiO_2(aq)$	35.7464
$HS^- + 2O_2(aq) \Leftrightarrow H^+ + SO_4^{2-}$	138.316
$H_6(H_2SiO_4)_4^{2-} + 2H^+ \Leftrightarrow 8H_2O + 4SiO_2(aq)$	13.4464
$HCl(aq) \Leftrightarrow H^+ + Cl^-$	0.6700
$HSO_4^- \Leftrightarrow H^+ + SO_4^{2-}$	1.9791

	$Al(OH)_4^- + 4H^+ \Leftrightarrow Al^{3+} + 4H_2O$	22.1477
	$Al(OH)_3(aq) + 3H^+ \Leftrightarrow Al^{3+} + 3H_2O$	16.1577
	$Al(OH)_2^+ + 2H^+ \Leftrightarrow Al^{3+} + 2H_2O$	10.0991
	$AlOH^{2+} + H^+ \Leftrightarrow Al^{3+} + H_2O$	5.0114
	$H_2(aq) + 0.5O_2(aq) \Leftrightarrow H_2O$	46.10
	$Fe(OH)_2^+ + 2H^+ \Leftrightarrow Fe^{2+} + 2H_2O$	5.6700
	$Fe(OH)_2(aq) + 2H^+ \Leftrightarrow Fe^{2+} + 2H_2O$	20.600
	$Fe(OH)_3(aq) + 3H^+ \Leftrightarrow Fe^{3+} + 3H_2O$	12.1728
	$Fe(OH)_4^- + 4H^+ \Leftrightarrow Fe^{3+} + 4H_2O$	21.600
	$Fe^{3+} + 0.5H_2O \Leftrightarrow 0.25O_2(aq) + Fe^{2+} + H^+$	-8.490
	$FeCO_3(aq) \Leftrightarrow Fe^{2+} + CO_3^{-2}$	-4.730
	$FeHCO_3^+ \Leftrightarrow Fe^{2+} + HCO_3^-$	-2.050
	$FeC^+ \Leftrightarrow Fe^{2+} + Cl^-$	0.1605
	$FeCl^{2+} \Leftrightarrow Fe^{3+} + Cl^-$	0.8108
	$FeOH^+ + H^+ \Leftrightarrow Fe^{2+} + H_2O$	10.8950
	$FeOH^{2+} + H^+ \Leftrightarrow Fe^{3+} + H_2O$	4.3815
	$FeSO_4(aq) \Leftrightarrow Fe^{2+} + SO_4^{2-}$	-2.2000
	$Fe_2(OH)_2^{4+} + 2H^+ \Leftrightarrow 2Fe^{3+} + 2H_2O$	7.2826
Minerals		**LogK (25°C)**
Brucite	$Mg(OH)_2(s) \Leftrightarrow Mg^{2+} + 2H_2O - 2H^+$	16.30
Calcite	$CaCO_3(s) + H^+ \Leftrightarrow Ca^{2+} + HCO_3^-$	1.85
Gyrolite	$Ca_2Si_3O_8{:}2.5H_2O(s) + 4H^+ \Leftrightarrow 2Ca^{2+} + 3SiO_2(aq) + 4.5H_2O$	22.91
Tobermorite	$Ca_5Si_6O_{17}{:}10.5H_2O(s) + 10H^+ \Leftrightarrow 5Ca^{2+} + 6SiO_2(aq) + 15.5H_2O$	63.84
Quartz	$SiO_2(s) \Leftrightarrow SiO_2(aq)$	–4.00
Dolomite	$CaMg(CO_3)_2(s) + 2H^+ \Leftrightarrow Ca^{2+} + Mg^{2+} + 2HCO_3^-$	4.06
Portlandite	$Ca(OH)_2(s) + 2H^+ \Leftrightarrow Ca^{2+} + 2H_2O$	22.55
Sepiolite	$Mg_4Si_6O_{15}(OH)_2{:}6H_2O(s) + 8H^+ \Leftrightarrow 4Mg^{2+} + 6SiO_2(aq) + 11H_2O$	30.44
Gypsum	$CaSO_4{:}2H_2O(s) \Leftrightarrow Ca^{2+} + SO_4^{2-} + 2H_2O$	–4.48
Ettringite	$Ca_6Al_2(SO_4)_3(OH)_{12}{:}26H_2O(s) + 12H^+ \Leftrightarrow 2Al^{3+} + 3SO_4^{2-} + 6Ca^{2+} + 38H_2O$	60.81
Fe(s)	$Fe(s) + 2H^+ + 0.5O_2(aq) \Leftrightarrow Fe^{2+} + H_2O$	59.03
Magnetite	$Fe_3O_4(s) + 8H^+ \Leftrightarrow Fe^{2+} + 2Fe^{3+} + 4H_2O$	10.47
Siderite	$FeCO_3(s) + H^+ \Leftrightarrow Fe^{2+} + HCO_3^-$	-0.19
Goethite	$FeO(OH)(s) + 2H^+ \Leftrightarrow Fe^{2+} + 1.5H_2O + 0.25O_2(aq)$	0.53
Smectite	$K_{0.055}Na_{0.135}Ca_{0.125}Mg_{0.1}(Al_{1.545}Mg_{0.425})(Si_{3.86}Al_{0.145})O_{10}(OH)_2(s) + 6.56H^+ \Leftrightarrow 0.135Na^+ + 0.055K^+ + 0.125\,Ca^{2+} + 0.525Mg^{2+} + 1.69\,Al^{3+} + 3.86SiO_2(aq) + 4.28H_2O$	6.26
Analcime	$Na_{0.96}Al_{0.96}Si_{2.04}O_6{:}H_2O(s) + 4H^+ \Leftrightarrow 0.96Al^{3+} + Na^+ + 2SiO_2(aq) + 3H_2O$	6.78
Mg-saponite	$Mg_{3.165}Al_{0.33}Si_{3.67}O_{10}(OH)_2(s) + 7.32H^+ \Leftrightarrow 0.33Al^{3+} + 3.165Mg^{2+} + 3.67SiO_2(aq) + 4.66H_2O$	25.97
Cation exchange		**$K_{Na\text{-}cation}$**
	$Na^+ + X\text{-}K \Leftrightarrow K^+ + X\text{-}Na$	0.138 (0.094)
	$Na^+ + 0.5\,X_2\text{-}Ca \Leftrightarrow 0.5\,Ca^{2+} + X\text{-}Na$	0.2924 (0.279)
	$Na^+ + 0.5\,X_2\text{-}Mg \Leftrightarrow 0.5\,Mg^{2+} + X\text{-}Na$	0.2881 (0.306)
	$Na^+ + 0.5\,X_2\text{-}Fe \Leftrightarrow 0.5\,Fe^{2+} + X\text{-}Na$	0.5
Surface complexation		**Log K_{25}**
$S^SOH_2^+$	$\equiv S^SOH_2^+ \Leftrightarrow \equiv S^SOH + H^+$	-4.5
S^SO^-	$\equiv S^SO^- + H^+ \Leftrightarrow \equiv S\,^SOH$	7.9
S^SOFe^+	$\equiv S^SOFe^+ + H^+ \Leftrightarrow \equiv S^SOH + Fe^{2+}$	0.6
S^SOFeOH	$\equiv S^SOFeOH \Leftrightarrow \equiv S^SOH + Fe^{2+} - 2H^+ + H_2O$	10.0
$S^SOFe(OH)_2^-$	$\equiv S^SOFe(OH)_2^- \Leftrightarrow \equiv S^SOH + Fe^{2+} - 3H^+ + 2H_2O$	20.0
$S^{w1}OH_2^+$	$\equiv S^{W1}OH_2^+ \Leftrightarrow \equiv S^{W1}OH + H^+$	-4.5
$S^{w1}O^-$	$\equiv S^{W1}O^- + H^+ \Leftrightarrow \equiv S^{W1}OH$	7.9
$S^{w1}OFe^+$	$\equiv S^{w1}OFe^+ \Leftrightarrow \equiv S^{W1}OH + Fe^{2+} - H^+$	3.3
$S^{w2}OH_2^+$	$\equiv S^{W2}OH_2^+ \Leftrightarrow \equiv S^{W2}OH + H^+$	-6.0
$S^{w2}O^-$	$\equiv S^{W2}O^- + H^+ \Leftrightarrow \equiv S^{W2}OH$	+10.5

Table 2. Thermal and hydrodynamic parameters of the canister, the bentonite barrier, the concrete liner and the clay formation.

Parameter	Carbon steel canister (assumed)	Bentonite barrier	Concrete liner	Clay formation
Hydraulic conductivity (m/s)	$2.75 \cdot 10^{-14}$	$2.75 \cdot 10^{-14}$	$3.39 \cdot 10^{-12}$	$4.19 \cdot 10^{-12}$
Initial porosity	0.407	0.407	0.085	0.37
Effective diffusion (m^2/s)	$4.08 \cdot 10^{-11}$	$4.08 \cdot 10^{-11}$	$8.56 \cdot 10^{-12}$	$5.01 \cdot 10^{-11}$
Density of the solids (kg/m^3)	7860	2700	2513	2778
Specific heat capacity (J/kg ^oK)	477.66	846.4	1374.32	1118.7

Table 3. Thickness of the bentonite and the clay formation affected by a decrease in porosity of 15%, 50% and 100% (clogging) at the bentonite-canister interface, in the bentonite near the concrete interface and in the clay near the concrete interface. The numbers within parentheses indicate the number of elements in the bentonite or in the clay affected by a decrease in porosity.

Time (years)	Affected thickness (cm)								
	Bentonite-canister interface			Bentonite near the concrete interface			Clay near the concrete interface		
	Porosity decrease > 15%	Porosity decrease > 50%	Pore clogging	Porosity decrease > 15%	Porosity decrease > 50%	Pore clogging	Porosity decrease > 15%	Porosity decrease > 50%	Pore clogging
10^3	0	0	0	0	0	0	2.50 (3)	1.67 (2)	0
10^4	1 (1)	1 (1)	0	0	0	0	2.50 (3)	2.50 (3)	1.67 (2)

10^5	5.03 (3)	2.53 (2)	1 (1)	0	0	0	4.17 (5)	2.50 (3)	1.67 (2)
10^6	75.03 (30)	2.53 (2)	1 (1)	75.03 (30)	0	0	6.67 (7)	4.17 (5)	3.33 (4)